Heteronuclear DNP of ^{1}H and ^{19}F nuclei using BDPA as a polarizing agent

Antonio Gennaro, Alexander Karabanov, Alexey Potapov and Walter Köckenberger*
School of Physics and Astronomy, University of Nottingham, University Park, Nottingham,

NG7 2RD, UK

**corresponding author: alexey.potapov@nottingham.ac.uk, tel. +44 115 951 4739*

Abstract

This work explores the dynamic nuclear polarization (DNP) of ^{1}H and ^{19}F nuclei in a sample of 25/75 (% v/v) fluorobenzene/toluene containing the radical 1,3-bisphenylene-2-phenylallyl radical (BDPA) as a polarizing agent. Previously, heteronuclear effects in DNP were studied by analysing the shapes of DNP spectra, or by observing cross-relaxation between nuclei of different types. In this work, we report a rather specific DNP spectrum, where ^{1}H and ^{19}F nuclei obtain polarizations of opposite signs upon microwave (MW) irradiation. In order to explain this observation, we introduce a novel mechanism called heteronuclear thermal mixing (hn-TM). Within this mechanism the spectra of opposite signs can then be explained due to the presence of four-spin systems, involving a pair of dipolar coupled electron spins and hyperfine coupled nuclear spins of ^{1}H and ^{19}F, such that a condition relating their Larmor frequencies $|\omega_{1e} - \omega_{2e}| \approx \omega_H - \omega_F$ is satisfied. Under this condition, a strong mixing of electron and nuclear states takes place, enabling simultaneous four-spin flip-flops. Irradiation of electron spin transitions with MW followed by such four-spin flip-flops produces non-equilibrium populations of $|\alpha_H\beta_F\rangle$ and $|\beta_H\alpha_F\rangle$ states, thus leading to the enhancements of opposite signs for ^{1}H and ^{19}F. Signal enhancements, build-up times and DNP-spectra as a function of MW power and polarizing agent concentration, all provide additional support for assigning the observed DNP mechanism as hn-TM and distinguishing it from other possible mechanisms.

We also develop a quantum mechanical model of hn-TM based on averaging of spin Hamiltonians. Simulations based on this model show very good qualitative agreement with experimental data. In addition, the system exhibits cross-relaxation between ^{1}H and ^{19}F induced by the presence of BDPA, which was detected by measuring the ^{19}F signal build-up upon saturation of ^{1}H nuclei with a train of radio-frequency pulses. We demonstrate that such cross-relaxation most likely originates due to the same electron and nuclear states mixing in the four-spin systems.

Introduction

Dynamic Nuclear Polarization (DNP) allows increasing the nuclear magnetic resonance (NMR) signals by transferring large polarization of electron spins onto coupled nuclear spins via microwave (MW) irradiation. Signal enhancements due to DNP are widely used to improve the sensitivity of solid state and solution NMR spectroscopy[1,2], as well as medical magnetic resonance imaging[3]. In many of these applications, the studied samples contain more than one type of polarizable nuclei, further referred to as heteronuclei. The presence of heteronuclei affects the DNP spectra, where the signal enhancements are recorded as a function of MW frequency applied to the system. Furthermore, in systems with heteronuclei the presence of unpaired electrons induces a polarization exchange between nuclei of different types, thereby indirectly affecting the dynamics of their polarization build-up in the DNP experiments. Understanding the mechanisms of these heteronuclear effects is therefore important for the ultimate goal of obtaining the optimal conditions for DNP.

Lots of insights into these heteronuclear effects were previously obtained by extending the main physical mechanisms known to produce DNP in non-conducting solids, such as solid effect (SE)[4–7], cross-effect (CE)[5,8] and thermal mixing (TM)[4,5]. One such mechanism involving two types of polarizable nuclei is a double-solid effect (double-SE), which can be explained using a simple quantum mechanical model involving three spins: one electron and two nuclei. There, MW irradiation applied to the relevant "forbidden" transitions can simultaneously flip all three spins. Such phenomenon has been first observed experimentally by de Boer in a sample of deuterated m-xylene-d6 doped with 1,3-bisphenylene-2-phenylallyl radical (BDPA) as a polarizing agent in a magnetic field of 2.5 T[9]. In addition to conventional SE, the DNP spectrum there had features centred at the MW irradiation frequencies $\omega_{MW} = \omega_e + \omega_H \pm \omega_D$ and $\omega_{MW} = \omega_e - \omega_H \pm \omega_D$, where ω_H, ω_D and ω_e are the Larmor frequencies of ^{1}H, ^{2}H and electrons respectively.

The theory of thermal mixing uses thermodynamic approach to explain DNP. In this mechanism, MW irradiation lowers the temperature of the energy reservoir formed by the electron spin dipolar interactions. DNP arises as a result of the energy exchange between this dipolar reservoir with nuclear Zeeman energy reservoirs. Under conditions of slow energy exchange with the lattice, this process produces the same temperature across all nuclear reservoirs, as can be experimentally confirmed by similar shapes of their DNP spectra[9–15]. On the other hand, nuclear Zeeman reservoirs are coupled to the electron spin dipolar reservoir regardless of the applied MW irradiation. Therefore, thermodynamically speaking, the two types of nuclei are in the indirect thermal contact with one another, leading to an observable polarization exchange between the two[11,16]. Recently, however, thermal mixing was also treated using models based on density matrix formalism[17,18]. In particular, the emergence of a common spin temperature in the dipolar reservoir of strongly coupled electron spins has been confirmed by the simulations[17], which provides support for this concept, crucial to the thermodynamic description of TM-mechanism. However, no effective quantum mechanical treatment of TM in a heteronuclear system has been presented so far.

The effect of two types of polarizable nuclei has been considered quantum mechanically in a system containing two electrons, one coupled ^{1}H and one coupled ^{13}C nuclei[19]. In addition to the conventional SE and CE mechanisms expected for this system, that work predicted an existence of a four-spin mechanism called {^{1}H,^{13}C}-heteronuclear-cross-effect (hn-CE). There, a pair of levels becomes degenerate when the difference of the two electron Larmor frequencies (denoted by ω_{1e} and ω_{2e}) is matched by a sum or difference of the two nuclear Larmor frequencies, i.e. $|\omega_{1e} - \omega_{2e}| \approx |\omega_H \pm \omega_C|$, where ω_H and ω_C are the Larmor frequencies of ^{1}H and ^{13}C respectively. In particular, in a hypothetic system with two narrow electron lines centred at frequencies ω_{1e} and ω_{2e}, such that $|\omega_{1e} - \omega_{2e}| \approx \omega_H - \omega_C$ and $\omega_{1e} < \omega_{2e}$, irradiation at $\omega_{MW} \approx \omega_{1e}$ produces positive enhancement for ^{1}H nuclei and negative

enhancement for ^{13}C nuclei. In turn, irradiation at $\omega_{MW} \approx \omega_{2e}$ produces negative enhancement for ^{1}H and positive enhancement for ^{13}C nuclei. However, to the best of our knowledge no experimental data clearly showing such DNP spectrum have been presented so far.

Kaminker et al. have discovered that DNP spectra of ^{2}H nuclei have the same shape as the DNP spectra of ^{1}H-nuclei arising due to the CE mechanism in a system with a nitroxide radical as a polarizing agent (magnetic field ~3.4 T, temperature 6 K)[20]. In addition, they observed a polarization transfer between ^{1}H and ^{2}H nuclei in an experiment which follows the recovery of ^{2}H signals, starting with saturated ^{2}H nuclei and highly polarized ^{1}H nuclei. The recovery curves show a characteristic overshoot, where ^{2}H nuclei quickly achieve polarization larger than thermal due to their cross-relaxation with ^{1}H. This high polarization then slowly decays towards the thermal equilibrium. TM-mechanism cannot provide an adequate explanation of these experiments, because as shown previously, the DNP in such systems arises due to the SE and CE[21]. The observed nuclear cross-relaxation can instead be explained using a four-spin model developed in ref.[19] by pointing out that the electron and nuclear state mixing in a four-spin system takes place regardless of the applied MW irradiation. Therefore the non-equilibrium polarization in one type of nuclei can get transferred to the nuclei of another type by means of electrons pairs satisfying the hn-CE matching condition. The same four-spin mechanism may also potentially play a role in a previously observed cross-relaxation between nuclei of different types such as ^{1}H and ^{13}C, ^{1}H and ^{15}N,^{1}H and ^{31}P taking place at a field of 6.7 T and a temperature of 4.2 K in the presence of a nitroxide as a polarizing agent[22].

In this work we investigate DNP of ^{1}H and ^{19}F nuclei in a toluene/fluorobenzene mixture using BDPA as a polarizing agent at the temperature of ~1.4 K and the magnetic field of 3.4 T. The narrow electron spin resonance (ESR) linewidth of BDPA (FWHH≈21 MHz for small BDPA concentrations) combined with a small difference in the nuclear Larmor frequencies ($\omega_H/2\pi$ =142.7 MHz for ^{1}H and $\omega_F/2\pi$ =134.2 MHz for ^{19}F) enables easy discrimination of

different DNP mechanisms in the DNP spectra. In addition to the conventional SE, the ^{1}H DNP spectrum features positive and negative enhancements below and above central frequency of $\omega_e/2\pi \approx$93.93 GHz respectively. However, the ^{19}F DNP spectrum follows the same shape with the opposite sign. As explained above, a rather similar spectrum has been previously predicted for the hn-CE mechanism[19], but now we present the first experimental evidence of it. Such heteronuclear DNP spectrum is explained by the presence of four-spin systems, where a flip-flop of the two electrons can cause a flip-flop of both ^{1}H and ^{19}F nuclei. For being effective, this process of energy transfer from electrons to nuclei requires a polarization gradient across the ESR line produced by MW irradiation. We develop a quantum mechanical description based on the averaging of spin Hamiltonians, which explains the emergence of such a polarization gradient, and show that the most likely mechanism for it in our system is thermal mixing. The assignment of the observed DNP spectra to this heteronuclear thermal mixing (hn-TM) is also supported by analysing the build-up times, enhancements and their power dependence. Simulations based on the developed quantum mechanical model show very good qualitative agreement with experimental data and provide additional support for ruling out hn-CE mechanism in favour of hn-TM. In addition, we observe, that the presence of electrons in the system produces a cross-relaxation between ^{1}H and ^{19}F nuclei, as was confirmed by saturation recovery experiments with and without saturation of ^{1}H nuclei with radiofrequency (RF) pulses. This cross-relaxation is attributed to the same four-spin process.

Theoretical background

Qualitative model of heteronuclear DNP

Heteronuclear-DNP (hn-DNP) effects have been analysed in detail by Shimon et al. using a four-spin model consisting of two electrons, one ^{1}H and one ^{13}C nucleus[19]. To analyse our experimental observations, we start by here by taking a similar approach, which we further

extend to take into account the collective effect of electron spin couplings. In our four-spin model system ^{1}H nuclei with Larmor frequency ω_H are found on the radical molecules BDPA and the solvent molecules, whereas ^{19}F nuclei with a Larmor frequency ω_F, belong to fluorobenzene molecules, taking on the role of the ^{13}C nuclei in Shimon et al.'s work. The two electrons with Larmor frequencies ω_{1e}, ω_{2e} are located on two different BDPA radical molecules and we assume for definiteness that $\omega_{1e} > \omega_{2e}$, with the frequency difference arising from the differences in their electronic g-tensors. The diagram in Fig. 1A shows schematically the sixteen energy levels for the corresponding unperturbed quantum states, where dashed boxes mark the manifolds of levels corresponding to the four electron states $|\alpha_{1e}\alpha_{2e}\rangle, |\beta_{1e}\alpha_{2e}\rangle, |\beta_{1e}\beta_{2e}\rangle, |\alpha_{1e}\beta_{2e}\rangle$. We ignore in this diagram any shifts of energy levels due to hyperfine and electron dipolar interactions. If the difference of the electron Zeeman interactions is $|\omega_{1e} - \omega_{2e}| \approx |\omega_H - \omega_F|$, a degeneracy occurs between some levels of the $|\alpha_{1e}\beta_{2e}\rangle, |\beta_{1e}\alpha_{2e}\rangle$ manifolds as shown in Fig. 1B. This degeneracy allows strong mixing of the corresponding populations mediated by an indirect interaction, which is made of the pseudosecular part of the nuclear hyperfine interactions with at least one of the electrons and the dipolar coupling between the two electrons. There are two scenarios for degenerate energy levels occurring in the four-spin model system:

a) When a condition $\omega_{1e} - \omega_{2e} \approx \omega_H - \omega_F$ is fulfilled, the two levels $|\alpha_{1e}\beta_{2e}\alpha_H\beta_F\rangle, |\beta_{1e}\alpha_{2e}\beta_H\alpha_F\rangle$ become degenerate and their populations get equilibrated due to the indirect interaction mentioned above.

b) When $\omega_{1e} - \omega_{2e} \approx -\omega_H + \omega_F$, in a similar manner the populations of the two levels $|\alpha_{1e}\beta_{2e}\beta_H\alpha_F\rangle$, $|\beta_{1e}\alpha_{2e}\alpha_H\beta_F\rangle$ get equilibrated.

In either of the two scenarios the perturbation of the thermal populations by the application of a microwave field at $\omega_{mw} \approx \omega_{1e}$ produces large non-equilibrium gradients between the

populations of the $|\beta_H\alpha_F\rangle$ and $|\alpha_H\beta_F\rangle$ states, i.e. positive enhancements for ^{19}F and negative enhancements for ^{1}H. On the other hand, irradiation at $\omega_{mw} \approx \omega_{2e}$ changes the sign of these population gradients and negative enhancements for ^{19}F and positive enhancements for ^{1}H are generated. Since the ESR linewidth of BDPA is much narrower than $(\omega_H + \omega_F)$, degeneracies at $|\omega_{1e} - \omega_{2e}| \approx \omega_H + \omega_F$ are irrelevant, and only the matching condition $|\omega_{1e} - \omega_{2e}| \approx \omega_H - \omega_F$ is important. In principle, such minimal model, identical to the hn-CE model developed earlier[19], can explain the transfer of electron polarisation to the two interacting nuclei. However, the significant shift between the electron spin frequencies requires a sufficiently strong g-anisotropy, which as we show later, is not entirely true for the narrow ESR line of BDPA.

Another possibility for the creation of the frequency shift between the electrons arises if the model is extended to include many strongly dipolar coupled electron spins. As Fig. 1C illustrates, in this scenario the electron levels split into bands, corresponding to a projection of the total electron angular momentum $|M_S\rangle$, while the energy difference between these bands is ~ω_e – the central frequency of the ESR line. The characteristic width of a band Δ_{band} arises primarily due to dipolar couplings between electrons but could also have contributions due to differences in g-values and hyperfine interactions. A pair of ^{1}H and ^{19}F nuclei coupled to such an electronic system produces splitting in these bands as shown in Fig. 1C. In our system the ESR linewidth of BDPA (FWHH≈21 MHz) is comparable to the difference of nuclear Larmor frequencies $(\omega_H - \omega_F)/2\pi \approx 8.4$ MHz, therefore $\Delta_{band} \gtrsim \omega_H - \omega_F$, which leads to a rather strong overlap between the bands corresponding to $|\alpha_H\beta_F\rangle$ and $|\beta_H\alpha_F\rangle$ nuclear states. In the hn-CE model above we explained that due to the ^{1}H and ^{19}F pseudosecular hyperfine couplings and electron dipolar coupling, a noticeable mixing of levels between the $|\alpha_H\beta_F\rangle$ and $|\beta_H\alpha_F\rangle$ bands can take place. In the extended model which includes many strongly coupled electrons, these levels effectively form one combined band, where the application of MW irradiation

creates a non-equilibrium distribution of populations between the levels. An electron pair within this band with the appropriate frequency difference could in analogy to the hn-CE model produce non-equilibrium populations of $|\alpha_H\beta_F\rangle$ and $|\beta_H\alpha_F\rangle$ states. The important difference between the hn-CE model and this extended model is the origin of electron frequency shift. In the extended model it arises due to the dipolar interactions of the electrons with the remaining dipolar electron network. Such a scenario is equivalent to a thermal mixing DNP model, where the electron dipolar reservoir is coupled to a Zeeman reservoir of a fictitious spin $I = 1/2$ formed by the two levels $|\alpha_H\beta_F\rangle$ and $|\beta_H\alpha_F\rangle$. We further refer to this model of DNP as heteronuclear thermal mixing (hn-TM). The next section takes a more rigorous quantum mechanical approach to describe the DNP in this heteronuclear system.

Quantum mechanical model of heteronuclear DNP

We consider a system of dipolar coupled unpaired electron spins $\mathbf{S}_j$, $j = 1, \dots, N$, localized on different BDPA radical molecules. Each of the electrons "j" also interacts with two different groups of nuclear spins, an ensemble of ^{1}H nuclear spins $\mathbf{I}_j^{(k)}$, $k = 1, \dots, n$, some of which belong to a BDPA molecule, as well as several nuclear ^{19}F spins $\mathbf{J}_j^{(l)}$, $l = 1, \dots, m$, which in our case belong to the solvent fluorobenzene molecules. Focusing on the direct electron-nuclear polarization exchange, we ignore nuclear spins of both species that are far from the electrons and gain their polarization only via spin diffusion from other nuclei. The electron spin ensemble is irradiated with a microwave field of a strength ω_1. The effective Hamiltonian written in the microwave rotating frame has the form:

$$\hat{H} = \hat{H}_0 + \hat{H}_{\mathrm{mw}} + \hat{H}_{\mathrm{en}}, \qquad (1)$$

where $\hat{H}_{\mathrm{mw}}$ describes the microwave irradiation energy, $\hat{H}_{\mathrm{en}}$ describes the semi-secular hyperfine (HF) interaction energy, and $\hat{H}_0$ contains the electron and nuclear Zeeman

interaction energies, the secular HF interaction energy and the energy of the mutual electron dipolar coupling. Specifically, the $\hat{H}_{\mathrm{mw}}$ and $\hat{H}_{\mathrm{en}}$ have the form:

$$\hat{H}_{\mathrm{mw}} = \frac{\omega_1}{2}\sum_j \left(\hat{S}_{j+} + h.c.\right) \tag{2}$$

$$\hat{H}_{\mathrm{en}} = \frac{1}{2}\sum_j \left[\sum_k B_{kj}^{(H)} \hat{I}_{j+}^{(k)} + \sum_l B_{lj}^{(F)} \hat{J}_{j+}^{(l)} + h.c.\right] \hat{S}_{jz}, \tag{3}$$

where $B_{kj}^{(H)}, B_{lj}^{(F)}$ are the semi-secular hyperfine interactions of ^{1}H and ^{19}F nuclei respectively, and $h.c.$ stands for Hermitian conjugates of the operators. The summation over "j" in eqn (2) and (3) is carried out over all electrons in the system, while summation over "k" and "l" in eqn(3) is carried out over all nuclei coupled to the electron spin "j". The Hamiltonian term $\hat{H}_0$ can be conveniently split into two parts, where $\hat{\tilde{H}}_0$ represents the Zeeman part , and $\hat{H}^0$ are the remaining terms:

$$\hat{H}_0 = \hat{\tilde{H}}_0 + \hat{H}^0 \tag{4}$$

$$\hat{\tilde{H}}_0 = \sum_j \left[\Delta \hat{S}_{jz} + \omega_H \sum_k \hat{I}_{jz}^{(k)} + \omega_F \sum_l \hat{J}_{jz}^{(l)}\right] \tag{5}$$

$$\hat{H}^0 = \sum_j \left[\Delta_j^g + \sum_k A_{kj}^{(H)} \hat{I}_{jz}^{(k)}\right] \hat{S}_{jz} + \sum_{j<j'} D_{jj'}(3\hat{S}_{jz}\hat{S}_{j'z} - \hat{\mathbf{S}}_j \hat{\mathbf{S}}_{j'}) \tag{6}$$

Here $\Delta = \omega_{MW} - \omega_e$ denotes the offset of the microwave frequency ω_{MW} from the centre of the electron resonance line ω_e. In addition, $\Delta_j^{(g)} = \omega_j - \omega_e$ are the electron frequency shifts due to g-anisotropy, $A_{kj}^{(H)}$ are the strengths of secular hyperfine interactions of ^{1}H nuclei, and $D_{jj'}$ is the mutual dipolar electron spin interaction strengths. For simplicity, we neglect the ^{19}F hyperfine secular interaction as this species is remote from the electrons. We also neglect the dipolar interactions between the considered nuclear spins as they are too weak compared to other interactions. Eqn (6) describes the broadening of ESR line. There, the first term is

responsible for inhomogeneous broadening due to g-anisotropy and hyperfine couplings, whereas the second term describes homogeneous broadening due to electron spin dipolar couplings.

In this system there are several possible mechanisms for polarisation transfer between electrons and nuclear spins. In the simplest case polarisation transfer can be mediated by SE DNP between an electron $\mathbf{S}_j$ and its coupled ^{1}H nuclei $\mathbf{I}_j^{(k)}$ as well as between the same electron and its coupled ^{19}F nuclei $\mathbf{J}_j^{(k)}$ if the corresponding SE condition $|\omega_{MW} - \omega_e| \approx \omega_H, \omega_F$ is met[4–7].

Since the ESR linewidth of BDPA radicals is much smaller than the Larmor frequencies of both ^{1}H and ^{19}F nuclei, the difference of electron Larmor frequencies ω_{1e}, ω_{2e} does not match any of those nuclear frequencies as needed for conventional CE[5,8], i.e. $|\omega_{1e} - \omega_{2e}| \neq \omega_H, \omega_F$. On the other hand, the ESR linewidth is wide enough to fulfil the condition for the hn-CE, i.e. $|\omega_{1e} - \omega_{2e}| \approx |\omega_H - \omega_F|$. In this case, the polarisation transfer is mediated by an energy conserving four-spin flip-flop that involves two electrons, one ^{1}H and one ^{19}F nucleus. There, the difference of electron polarisations between electron spins is transferred to the nuclear spin pair. However, such four-spin flip-flops can also be brought about by the heteronuclear thermal mixing (hn-TM) which was qualitatively described above. The properties of the electron spin system, such as the strength of interactions and the timescales of relaxation processes, determine which of the two mechanisms would dominate. The strength of the two terms in $\widehat{H}^0$ becomes of particular importance. As pointed out earlier, the first term in $\widehat{H}^0$ describes the inhomogeneous broadening, whereas the second term describes the mutual electron spin dipolar interactions. Qualitatively, in the CE mechanism, the inhomogeneous broadening (i.e. the first term) is large enough to treat the evolution under the dipolar interactions (i.e. the second term) as a perturbation. In contrast, under TM mechanism, the evolution of the spin

system is dominated by the mutual electron dipolar interactions, whereas the first term acts only as a perturbation.

The Electronic Supplementary Information (ESI) provides the details of a procedure for averaging eqn (1) in order to obtain an effective Hamiltonian representing the macroscopic electron-nuclear dynamics arising due to the different possible DNP mechanisms. The two necessary key steps of this procedure are the transformation of eqn (1) to a frame rotating with zero-quantum spin transitions and the adiabatic elimination of oscillating non-secular terms. The calculations of effective Hamiltonians for SE, hn-CE and hn-TM were carried out, and a summary of those calculations for the hn-TM pathway is presented below.

The hn-TM mechanism can be described by a minimal model Hamiltonian $\widehat{H}_{\mathrm{hnTM}}$ that involves two effective electrons $\mathbf{S}_1$ and $\mathbf{S}_2$ and two unlike nuclear spins **I** and **J**, which represent the spins of the ^{1}H and ^{19}F nuclei respectively. The effective Hamiltonian depends on the normalized ESR line shape $f(\Delta)$ and the dispersion parameter d, describing the effective frequency shift between the two neighbouring electrons. Such frequency shift arises due to different electron-electron dipolar interactions of the electrons $\mathbf{S}_1$ and $\mathbf{S}_2$ with the rest of the electronic spin ensemble, as well as due to differences of their g-values. However, the frequency shift is independent of the hyperfine couplings as shown in the "Properties of the spectral densities $f_j(\lambda)$ and $f'_{kj}(\lambda)$" section of the ESI. The effective Hamiltonian $\widehat{H}_{\mathrm{hnTM}}$ consists of a microwave term $\widehat{H}^{\mathrm{mw}}_{\mathrm{hnTM}}$ and a term $\widehat{H}^{\mathrm{en}}_{\mathrm{hnTM}}$ that represents the energy of the effective four-spin flip-flop process:

$$\widehat{H}_{\mathrm{hnTM}} = \widehat{H}^{\mathrm{mw}}_{\mathrm{hnTM}} + \widehat{H}^{\mathrm{en}}_{\mathrm{hnTM}} \tag{7}$$

$$\widehat{H}^{\mathrm{mw}}_{\mathrm{hnTM}} = \omega_1\left[f_+(\Delta)\hat{S}_{1x} + f_-(\Delta)\hat{S}_{2x}\right] \tag{8}$$

$$\hat{H}^{\mathrm{en}}_{\mathrm{hnTM}} = -\frac{DB_H B_F}{\omega_H \omega_F}\left[g_+ \hat{I}_+ \hat{J}_- \hat{S}_{1+} \hat{S}_{2-} + g_- \hat{I}_- \hat{J}_+ \hat{S}_{1+} \hat{S}_{2-}\right] + h.c. \qquad (9)$$

where D is the effective electron dipolar interaction strength and B_H, B_F are the effective pseudo-secular hyperfine interactions of the ^{1}H and ^{19}F nuclei respectively. In addition, $f_{\pm}(\Delta)$ and $g_{\pm}$ are the shorthand notations for:

$$f_{\pm}(\Delta) = f(\Delta \pm d) \qquad (10)$$

$$g_+ = \frac{1}{\nu}\int_0^{\infty} f_-(\Delta) f_+(\Delta - \omega_H + \omega_F) d\Delta \qquad (11)$$

$$g_- = \frac{1}{\nu}\int_0^{\infty} f_+(\Delta) f_-(\Delta - \omega_H + \omega_F) d\Delta, \qquad (12)$$

where normalization factor ν represents the average frequency gap between the multiple electron lines that arise from the secular hyperfine interaction of ^{1}H nuclei close to the electron.

As seen from eqn (8), application of MW irradiation saturates the two electrons $\mathbf{S}_1$ and $\mathbf{S}_2$ with different effective microwave field strengths for each of them. These effective strengths depend on the electron line shape function $f(\Delta)$ and the dispersion parameter d, and they ultimately lead to the creation of a polarisation gradient. This difference between polarizations of $\mathbf{S}_1$ and $\mathbf{S}_2$ is then transferred to the nuclear spins via the four-spin flip-flop described by the second Hamiltonian term $\hat{H}^{\mathrm{en}}_{\mathrm{hnTM}}$ in eqn (9). The strength of the spin flip-flop term is given by $\frac{DB_H B_F}{\omega_H \omega_F}$ and is modulated by the convolution integrals $g_{\pm}$ that differ in their magnitudes due to the effect of the dispersion parameter d. Because of that, the terms $\hat{I}_{\pm}\hat{J}_{\mp}\hat{S}_{1+}\hat{S}_{2-}$ have different effective strengths. In turn, they produce unequal amounts of $|\alpha_H \beta_F\rangle$ and $|\beta_H \alpha_F\rangle$ states and thus generate ^{1}H and ^{19}F enhancements of opposite signs.

The dispersion parameter d plays an important role of breaking the symmetry in the Hamiltonian by shifting one electron spin frequency with respect to the other, as was previously

discussed for regular TM mechanism[18]. When the dispersion parameter $d = 0$, the effective spin system Hamiltonian shown in eqns (7)(8)(9) is symmetric with respect to swapping $\mathbf{S}_1$ and $\mathbf{S}_2$ operators, making the two electron spins indistinguishable. As a result, when MW is applied to such a system, both $\mathbf{S}_1$ and $\mathbf{S}_2$ get saturated with the same effective MW strength as seen from eqn (8), so that the polarization difference required for the DNP cannot be created. Furthermore, when $d = 0$, parameters $g_{\pm}$ in eqn (9) have the same magnitude, with $\widehat{H}^{\mathrm{en}}_{\mathrm{hnTM}}$ producing no difference in nuclear polarizations. Such highly symmetric scenario with $d = 0$ however, can only be realized in an ideal single crystal without any heterogeneities. In any real sample, there are many heterogeneities, meaning that electron spin frequencies at each site are different leading to $d \neq 0$. In this case, the symmetry of the effective Hamiltonian with respect to swapping $\mathbf{S}_1$ and $\mathbf{S}_2$ is broken as seen in eqns (7)(8)(9). The departure from the highly symmetric case, described by the dispersion parameter d, is thus a very important characteristic of the system needed for producing the DNP.

The effective Hamiltonians for hn-TM and other DNP mechanisms can be used to derive the master equations for the density matrix in the Lindblad form, as shown in the "Density Matrix Simulations" section of the ESI. In these equations, the relaxation is taken into account using a standard approach with single-spin Markovian jump operators. The simulations based on these master equations will be compared to experimental data in the "Results" section. The calculations use various relaxation and other common parameters shown in Table 1. In addition, the ESR lineshape $f(\Delta)$ in these calculations is taken as a Gaussian, described by a full width at half height (FWHH) parameter A.

Materials and experiments

Sample preparation

The experiments were performed on samples containing various concentrations of BDPA (1,3-bisphenylene-2-phenylallyl) radicals in a solution of 75/25 (% v/v) of toluene ($C_6H_5CH_3$) and fluorobenzene (C_6H_5F). The materials were purchased from Sigma Aldrich, Inc. and used without additional purification. About 50 µl of liquid sample was placed into a shortened 4-mm capillary made of Wilmad quartz (CFQ) ESR tubes and loaded into the NMR probe. The probe was inserted into a cryostat precooled at about 130 K. After precooling the sample temperature was lowered further by increasing the helium flow and lowering the pressure by continuous vacuum pumping (see cryostat description below). For some experiments the samples were degassed using three freeze-pump-thaw cycles. The sample was i) frozen by dipping in liquid nitrogen, ii) the remaining gas was pumped out using a vacuum pump, iii) and finally, the sample was thawed and the normal pressure is restored by letting the nitrogen gas into the system.

Equipment

All experiments were performed using a NMR-DNP system described previously[23]. In brief, the magnet (Oxford Instrument, Abingdon, UK) produces a field of about 3.35 T, where the Larmor frequency of a free electron is about 94 GHz, and the Larmor frequencies of ^{1}H and ^{19}F are $\omega_H/2\pi$ =142.7 MHz and $\omega_F/2\pi$ =134.2 MHz respectively. The helium Dewar of the main magnet is connected to the sample space of the variable-temperature insert (VTI), where the NMR sample is placed. The flow of liquid helium into the VTI is controlled by a needle valve, while the level of liquid helium there can be monitored using a capacitive sensor (Oxford Instruments, Abingdon, UK). The sample space is filled with liquid helium (covering the NMR sample itself) and the pressure in the space above it is lowered by continuous pumping using a rotary pump (model DUO 65 M, Pfeiffer Vacuum, Aslar, Germany). Vacuum transducer

(model 720, Setra Systems Inc., Boxborough, MA) produces readings of the pressure in the sample space of the VTI which are being converted into temperature based on the tabulated values for liquid helium boiling point [24].

All the measurements were carried out at ~1.4 K. However, in this system it is difficult to find a needle valve opening position that produces stable helium level in the cryostat. Therefore, over the course of an experiment the liquid helium level changes, thereby affecting the heat flow in the system and the overall sample temperature. With a typical starting level of helium, the temperature varies by about ±0.1 K (as monitored by the pressure) over 1-2 hours, which is why the duration of most experiments was limited to this timescale. This ensures an acceptable variance in measured build-up times, which have rather significant temperature dependence in this temperature range. Repeated measurements of the ^{19}F nuclear effective longitudinal relaxation time T_{1F} in a sample containing 40 mM TEMPO radical (2,2,6,6-tetramethylpiperidine 1-oxyl, Sigma Aldrich, Inc.), produced 20% variance in the measured T_{1F} value (data not shown), which we use as an estimate for the accuracy of other obtained build-up time values. Turning on the MW irradiation at full power also produces additional boil off of liquid helium, which increases the temperature reading by ~0.1 K. Since the microwave losses in liquid helium are negligible[25], the boil off probably comes from the heat dissipation in the metallic walls of the chamber surrounding the sample.

The head of the NMR probe was made of brass, which together with the quartz material of the NMR capillary, where the sample is placed, does not contain any background signals of ^{1}H and ^{19}F. The probe was tuned to both ^{1}H and ^{19}F Larmor frequencies using an overcoupled tank circuit as described in refs.[26,27] While the coil is located at a cryogenic temperature, all other tuning and matching elements were placed at room temperature outside the magnet, and were connected via a transmission line, which length was adjusted to match about half of the wavelength at the ^{1}H frequency. The transmission line is a stainless steel semi-rigid coaxial

cable, with the dielectric insulating material made of PTFE (polytetrafluoroethylene) containing significant amount of ^{19}F. In order to avoid background ^{19}F signals the last 3 cm of the transmission line were replaced by a copper coated quartz capillary with a bare wire running coaxially.

The microwave source (Model VCOM-10, ELVA-1, St.Petersburg, Russia) has a maximum output of 400 mW at a controlled frequency in a range from 93.75 to 94.25 GHz. A microwave shield made of brass encloses a chamber around a sample. The shield has a circular opening through which the microwaves are delivered via an overmoded circular waveguide. Unless specifically stated otherwise, all DNP measurements were performed using the maximum MW output of 400 mW. Previously, ESR measurements were used to estimate the magnitude of the MW field produced at the location of a sample as $\omega_1/2\pi \sim$ 10 kHz for the source power of 400 mW[28].

The NMR measurements were carried out using a Bruker Avance 400 spectrometer, interfaced to a computer running the Topspin 1.3 software. The ^{19}F and ^{1}H pulses are produced using the same radiofrequency channel of the spectrometer, because the NMR probe had only a single input port for both ^{1}H and ^{19}F frequencies. Trigger pulses from the NMR spectrometer are routed into a NI-DAQ device (DAQPad-6016) interfaced with a LabVIEW (National Instruments) program, which controls the frequency, power and on/off state of the MW source via a serial port. The delays produced by the DAQ card, LabVIEW and MW source are negligible compared to the time intervals used in the NMR pulse programs and therefore did not affect the measurement results.

Results

DNP enhancements

Fig. 2A shows the ^{1}H and ^{19}F-DNP-spectra of a 25/75 (% v/v) fluorobenzene/toluene sample containing [BDPA]=40 mM. Recording of both spectra was done by interleaving the acquisition of ^{1}H and ^{19}F spectra, making a total of 100 steps in frequency. Each measurement begins with a train of saturating RF pulses for destroying the magnetization, i.e setting it to zero, which after delay is then followed by a readout pulse. The build-up time between this train and the readout pulse is set to $t_{bu} = 30$ s in order to limit the overall duration of the experiment. This ensures good temperature stability over its course, as explained in the Methods section. Since the magnetization build-up times for the DNP-effects are longer than 30 s (*vide infra*), the build-up of intensities in these spectra is incomplete.

The DNP spectra reveal positive and negative enhancements at the frequencies $(\omega_{MW} - \omega_0)/2\pi = \Delta/2\pi \approx \mp 132.4$ MHz respectively for ^{19}F and $(\omega_{MW} - \omega_0)/2\pi = \Delta/2\pi \approx \mp 142.7$ MHz respectively for ^{1}H, where $\omega_0/2\pi = 93.93$ GHz corresponds to the Larmor frequency of an unpaired electron in BDPA (g_{iso} ≈2.0026)[29]. These lines correspond to the SE DNP mechanism involving a single ^{19}F or ^{1}H nucleus. The ^{1}H DNP spectrum exhibits positive and negative enhancements at the frequencies $(\omega_{MW} - \omega_0)/2\pi \approx \mp 20$ MHz respectively. Previously, DNP spectra of ^{1}H in m-xylene-2,2-d6 doped with BDPA at 2.5 T magnetic field[9], were shown to exhibit a similar small feature explained by a rather inefficient thermal mixing mechanism, which could be the case for our measurements as well. However, the ^{19}F-DNP spectrum also shows negative and positive enhancements at the frequencies of $(\omega_{MW} - \omega_0)/2\pi \approx \mp 20$ MHz respectively. Such features have signs opposite to what is expected from a regular TM mechanism, and therefore cannot be explained by it.

Double-SE DNP mechanism involving a simultaneous flip of ^{1}H and ^{19}F nuclei is expected to produce positive enhancements at frequencies of $(\omega_{MW} - \omega_0)/2\pi = -(\omega_H + \omega_F)/2\pi \approx -277$ MHz and $(\omega_{MW} - \omega_0)/2\pi = (\omega_H - \omega_F)/2\pi \approx +8.4$ MHz, and negative enhancements at the frequencies $(\omega_{MW} - \omega_0)/2\pi = -(\omega_H - \omega_F)/2\pi = -8.4$ MHz, and $(\omega_{MW} - \omega_0)/2\pi = (\omega_H + \omega_F)/2\pi = +277$ MHz. Both positive and negative features are expected to have the same intensity[30]. Due to the bandwidth limit of our MW source the enhancements can only be observed in the region -180 MHz$< (\omega_{MW} - \omega_0)/2\pi <$320 MHz. However, as the spectrum reveals, the feature corresponding to $(\omega_{MW} - \omega_0)/2\pi = (\omega_H + \omega_F)/2\pi = +277$ MHz is not present in the spectrum, therefore features at $(\omega_{MW} - \omega_0)/2\pi = \mp 20$ MHz cannot be attributed to double-SE.

In contrast, four-spin models of heteronuclear DNP (hn-DNP), such as hn-CE developed by Shimon et al.[19] and hn-TM explained in the "Theoretical Background" section, agree better with the observed DNP spectrum. Both models rely on a strong mixing of electron and nuclear levels for ^{1}H and ^{19}F when electron frequencies differ by $|\omega_{1e} - \omega_{2e}| \approx \omega_H - \omega_F$. In both hn-CE and hn-TM scenarios, MW irradiation applied to an allowed ESR transition, followed by four-spin flip-flops, creates non-equilibrium populations of $|\alpha_H\beta_F\rangle$ and $|\beta_H\alpha_F\rangle$ states, thereby producing enhancements of opposite signs for ^{1}H and ^{19}F nuclei.

As pointed out in the "Theoretical Background" section the dominance of hn-TM or hn-CE mechanism is determined by the properties of the electron spin system, such as its homogeneous and inhomogeneous broadening and relaxation times. In order to help resolve the two mechanisms in our study, ESR spectra of BDPA at two concentrations were recorded using a high-field ESR spectrometer, as described in ESI. As can be seen in Fig. S1 of the ESI, for [BDPA]=1 mM the full ESR linewidth at half height FWHH≈21 MHz. By comparing our data with ESR spectra of deuterated-BDPA at 5 T measured by Weis and Griffin[31], the g-

anisotropy contribution can be estimated as 6 MHz, while the remaining 15 MHz of linewidth arises due to hyperfine couplings with nearby ^{1}H nuclei[29,32]. For higher concentration of [BDPA]=40 mM, the linewidth has an additional contribution due to the electron dipole-dipole couplings, giving FWHH≈27 MHz. Therefore, even at the high concentration, the ESR linewidth has both significant homogeneous and inhomogeneous broadening.

Previously, ^{1}H- and ^{2}H-DNP spectra in the presence of BDPA in deuterated m-xylene-d6 (magnetic field 2.5 T, temperature 0.5 K) have shown the positive and negative enhancements centred around the electron frequency ω_e, which were assigned to the thermal mixing effect[9]. The electron relaxation time for [BDPA]=80 mM in toluene at those experimental conditions was reported as T_{1e} ≈1.6 ms[9], which allows for rather efficient saturation of the entire ESR line via electron spectral diffusion, as detailed in the ESI. In addition, recent measurements of electron relaxation times in [BDPA]=15 mM (in 50:50 % v/v sulfolane:DMSO) at the magnetic field of 3.35 T and the temperature of 5 K, gave T_{1e} ≈0.1 s[33]. Extrapolating this result to 1.4 K, where our measurements are carried out, gives T_{1e} ≈0.3 s. Since the electron relaxation time is so long, the polarization gradient across the ESR line is not likely to emerge due to hole-burning with MW irradiation (as required by the CE), and mostly likely source of polarization gradient is the dynamic cooling of the electron dipolar reservoir as required by the TM mechanism.

Simulations using a quantum mechanical model outlined in the "Theoretical Background" section are shown in Fig. 2B. These calculations use a model based on effective Hamiltonians for hn-TM and SE and are shown with ^{1}H enhancement scaled by a factor $\chi = 0.6$. The appearance of this factor can be justified by the ^{1}H polarisation loss due to relaxation during transport of polarisation from the structural ^{1}H nuclei that are not observable to the observable bulk nuclei in the solvent. The top left panel of Fig. 2B shows the DNP spectra at 30 sec build-up, as done in the actual experiment. The top right panel of Fig. 2B shows the calculated DNP

spectra at 3000 sec build-up time, corresponding to spectra under steady-state conditions. The maximum DNP enhancements for SE and hn-DNP were measured in a separate experiment and shown in Table 2, they agree with enhancements appearing in simulated DNP spectra in the top right panel of Fig. 2B. The bottom left and bottom right panels of Fig. 2B show the same spectra with normalization to their maximum values. The bottom left panel represents normalized simulated DNP-spectra with a build-up of 30 sec, exactly as done in the experiment, and it shows a very good qualitative agreement with the experimental data in Fig. 2A.

To support further our assignment of SE and hn-DNP peaks, we explore the dependence of hn-DNP on the concentration of BDPA. The build-up times and enhancements extracted from the build-up curves of the samples with various BDPA concentrations are summarized in Table 2. The transition probability needed for the double-SE mechanism is smaller compared to regular SE, for that reason, the build-up time for the double-SE is expected to be noticeably longer than for regular SE[9,19]. As Table 2 shows, the build-up times for hn-DNP and SE-DNP are indeed different, yet have the same order of magnitude, which provides additional evidence that spectral lines assigned as hn-DNP cannot arise due to double-SE. The build-up times for SE and hn-DNP become shorter and enhancements increase with the concentration of the polarizing agent, and yet for hn-DNP the dependence is somewhat stronger. Since the SE mechanism involves excitation of only one electron, this concentration dependence qualitatively agrees with the fact that the hn-DNP process involves more than one unpaired electron spin. The build-up times of thermal signals were measured without MW irradiation. They also become shorter as the BDPA concentration increases, meaning that ^{19}F nuclear relaxation times are not dominated by the intrinsic processes, independent on the unpaired electrons. As we show later, in fact, the observed thermal signal build-ups rates depend significantly on the polarization transfer between ^{1}H and ^{19}F.

Fig. 3A shows a region of ^{19}F-DNP spectrum recorded at various concentrations of BDPA. While the shape of the SE remains almost the same regardless of the BDPA concentration, the positions of the largest (negative) enhancement for hn-DNP change with the BDPA concentration. Both SE and double-SE mechanisms are not expected to produce a significant effect on the shape of DNP spectrum as a function of BDPA concentration, because the shape of the ESR line is only slightly increased due to the presence of BDPA as shown in the Fig. S1 of the ESI. There is an additional contributing factor affecting the shape of DNP spectra for hn-TM and hn-CE mechanisms. The spectral shapes for both mechanisms are determined by a polarization profile produced upon a saturation of the ESR line. The latter in turn, depends on the strength of the dipolar couplings, i.e. concentration of the polarizing agent. In particular, the dipolar couplings define the width of a homogeneously broadened spin packet, but also determine the cross-relaxation rates between different packets in an inhomogeneously broadened line, both being critical for the thermal mixing and cross-effect mechanisms[5,34,35]. A clear change in the position of the negative enhancement feature in the DNP spectrum shape shown in Fig. 3A is therefore consistent with either hn-CE or hn-TM.

Simulations of hn-TM and SE as a function of BDPA concentration are shown in Fig. 3B. In terms of the quantum mechanical model described in the "Theoretical Background", the concentration affects the effective electron dipolar couplings that appear in eqn. (9). Furthermore, concentration affects the effective width of the ESR line $f(\Delta)$ and the dispersion parameter d, which depends on the couplings of electrons with other electrons in the ensemble. The top and bottom panels of Fig. 3B show the normalized DNP spectra simulated for 30 sec and 3000 sec of build-up respectively. The simulations are in a very good qualitative agreement with the experimental data shown in Fig. 3A. In addition, the simulations using a hn-CE model, based on an effective Hamiltonian derived in the ESI, are shown in Fig. 3C. There, the concentration dependence of the DNP spectral shape is noticeable, but not very pronounced.

Furthermore, the simulations show an increase of the enhancement up to the concentration of 8 mM, followed by a decrease for concentrations higher than that, in stark contrast with the experimental data. The simulations in Fig. 3B and 3C therefore provide support for hn-TM as a possible mechanism.

The DNP-enhancement of ^{19}F signals due to SE and hn-DNP were also measured at a 100 mW microwave power level for a sample with [BDPA]=30 mM, as shown in Table 2. A power decrease from 400 mW to 100 mW produces ~3.6±0.2 times smaller SE-enhancement, which shows that at 400 mW the SE DNP-effect has not yet reached a saturation. Double-SE enhancement involves forbidden transitions just as in a regular SE mechanism, and therefore a linear increase is expected at these typical power levels. In contrast, for ^{19}F hn-DNP the enhancement decreases only by a factor of 1.3±0.1, which points to the excitation of allowed transitions which get saturated at these power levels. In addition, the ^{19}F-DNP spectrum of the hn-DNP was recorded for several values of power as demonstrated in Fig. 4A. As power decreases from 400 mW to 4 mW, corresponding to a change of MW irradiation field from $\omega_1/2\pi\sim$ 10 kHz to $\omega_1/2\pi\sim$ 1 kHz, the shape of the DNP spectrum changes considerably. In particular, the interval between the maximum positive and negative enhancements gets smaller with a decrease of power, and the spectral wings obtain smaller intensity. Such a change again rules out the double-SE, which involves excitation of forbidden transitions, and off-resonant effects are expected to be small. However, the shape of the DNP spectrum due to TM and CE typically has a noticeable dependence on the power of the applied MW[35,36] due to the already mentioned dependence of these mechanisms on the electron spin polarization profile[5].

Fig. 4B shows the simulations of hn-TM as a function of MW ω_1 strength using the model described in the "Theoretical background". The simulated DNP-spectra qualitatively reproduce the decrease in the frequency interval between the maximum positive and negative enhancements observed in the experiments. Fig. 4C shows the ω_1 dependence of ^{19}F-DNP

spectra simulated using the hn-CE quantum mechanical model. The hn-CE model predicts no significant change in the shape of the DNP spectrum with the concentration of BDPA, in contrast to our experimental results. Furthermore, it fails to reproduce a rather significant intensity observed at the frequencies $|(\omega_{MW} - \omega_0)/2\pi| > 40$ MHz, which is very well represented by hn-TM model. Overall, these simulations provide additional evidence that the observed hn-DNP arises due to hn-TM mechanism.

^{1}H-^{19}F cross-relaxation

As pointed out in the "Theoretical Background" section, the strong mixing of electron and nuclear states in a four-spin system can produce cross-relaxation between the ^{1}H and ^{19}F nuclei regardless of the presence of MW irradiation. In order to probe this effect, ^{19}F saturation-recovery experiments were carried out with and without saturating pulses at the Larmor frequency of ^{1}H nuclei $\omega_{sat}/2\pi = \omega_H/2\pi$ =142.7 MHz. The pulse sequence used for this is shown in Fig. 5A. Saturation-recovery of the ^{19}F signal for a degassed sample of 25/75 (% v/v) fluorobenzene/toluene without paramagnetic dopant shows a gradual build-up as seen in Fig. 5B. While the time constants of the two curves are almost the same, the achieved equilibrium magnetization values are different. In order to test, whether such a change in the steady state magnetization is caused by an off-resonant excitation of ^{19}F nuclei by the pulses applied at $\omega_{sat}/2\pi$ =142.7 MHz, a control experiment was carried out, where the excitation frequency was set to $\omega_{sat}/2\pi$ = 138 MHz, away from ^{1}H and ^{19}F resonances. The build-up curves with and without such irradiation at $\omega_{sat}/2\pi$ =138 MHz coincide very well, demonstrating an absence of off-resonant effects. Therefore, the ^{19}F signal decrease upon ^{1}H saturation is caused by the cross-relaxation between ^{19}F and ^{1}H nuclei.

The ^{19}F signal build-up curves can be fitted using a simple model based on the Solomon equations[37], which is explained in the ESI. In the case when only zero-quantum cross-relaxation between ^{1}H and ^{19}F is active (i.e. double-quantum cross-relaxation for a ^{1}H-^{19}F pair is negligible), the evolution of nuclear polarizations in the experiments can be described by:

$$\frac{dP_F(t)}{dt} = -R_F\left[P_F(t) - P_{F,eq}\right] - \sigma[P_F(t) - P_H(t)] \tag{13}$$

$$\frac{dP_H(t)}{dt} = -R_H\left[P_H(t) - P_{H,eq}\right] + \sigma\frac{N_F}{N_H}[P_F(t) - P_H(t)] \tag{14}$$

where $P_F(t)$ and $P_H(t)$ are the polarizations of ^{19}F and ^{1}H respectively, R_F and R_H are intrinsic relaxation rates and σ is the effective cross-relaxation rate. Saturating ^{1}H nuclei with a train of radiofrequency (RF) pulses, reduces nuclear polarization to zero $P_H(t) = 0$, while no irradiation produces $P_H(t) = P_{H,eq}$. The solutions for the ^{19}F magnetization $P_F(t)$ describing polarization build-up with and without RF irradiation of ^{1}H nuclei can be obtained using eqn.(13):

$$P_F^{\text{with H}-\text{sat}}(t) = P_{F,eq}\left[1 - e^{-(R_F+\sigma)t}\right] \tag{15}$$

$$P_F^{\text{without H}-\text{sat}}(t) = \frac{R_F}{R_F+\sigma}P_{F,eq}\left[1 - e^{-(R_F+\sigma)t}\right] \tag{16}$$

In both cases, the magnetization builds up with the same time-constant $(R_F + \sigma)$ and the ratio of steady-state polarizations is given by:

$$\frac{P_F^{\text{with H}-\text{sat}}(\infty)}{P_F^{\text{without H}-\text{sat}}(\infty)} = \frac{R_F}{R_F+\sigma} \tag{17}$$

Table 3 summarizes the values R_F and σ obtained by fitting the build-up curves for samples with various concentrations of the polarizing agent. A non-degassed sample containing no polarizing agent exhibits a non-zero cross-relaxation between ^{1}H and ^{19}F. Degassing the sample decreases the cross-relaxation rate σ and the intrinsic relaxation rate R_F, demonstrating the contribution of the dissolved paramagnetic oxygen gas. However, a degassed sample still

exhibits a non-zero cross-relaxation of unknown origin. Increasing the polarizing agent concentration leads to an increase in the cross-relaxation rate σ, thus clearly confirming that crosstalk is induced by the presence of electrons. Interestingly, a sample containing [TEMPO]=40 mM, which has a broad ESR line (500 MHz at the base) has a R_F rate that is very similar to the one observed in [BDPA]=40 mM, but features a faster cross-relaxation rate σ. The possible reasons of this are discussed later.

In another experiment, which sequence is shown in Fig. S2A of the ESI, the recovery of ^{19}F signals was followed after turning off the MW irradiation and saturation of ^{19}F. In other words, the system evolution without MW irradiation starts with the "hot" (high spin temperature) ^{19}F nuclei and "cold" (low spin temperature) ^{1}H nuclei. The recovery of ^{19}F and ^{1}H signals for a sample with [BDPA]=40 mM is shown in Fig. S2B of the ESI. There, ^{1}H signals decay to thermal equilibrium with the rate close to the intrinsic R_H, while the ^{19}F signals quickly recover from zero to some value, which is higher than thermal equilibrium polarization $P_{F,eq}$, and then gradually decay to $P_{F,eq}$. Such behaviour is much more prominent in the sample containing [TEMPO]=40 mM, shown in Fig. S2C of the ESI, where the build-up of ^{19}F magnetization due to a flow of magnetization from polarized ^{1}H nuclei (determined by σ) is faster than its decay back to the thermal equilibrium value (determined by R_F). In principle, eqns.(13),(14) can be used to describe the behaviour of ^{1}H and ^{19}F polarization in this experiment, and R_H, R_F and σ parameters can be obtained by fitting the recovery curves. However, the fit parameters produced in this manner have rather large variance, especially for [BDPA]=40 mM sample, where R_F and σ are comparable in magnitude. Furthermore, the observed rates may be affected by a temperature change following the switching off of the MW irradiation.

Further evidence for a cross-relaxation between ^{19}F and ^{1}H can be observed in the DNP spectra of solid effect. Fig. S3 of the ESI shows the ^{1}H and ^{19}F signals as a function of microwave

irradiation with a finer step in MW frequency in the frequency range of $(\omega_{MW} - \omega_0)/2\pi$ =-180…-80 MHz. The ^{1}H DNP spectrum can be fitted with a single Gaussian line with FWHH≈27.9±0.4 MHz (centred at 143.5±0.3 MHz), which is in very good agreement with the shape expected based on ESR measurements (FWHH≈27.3±0.3 MHz). At the same time, fitting the ^{19}F DNP spectrum with a single Gaussian line produces a line with FWHH≈34.2±0.7 MHz (centred at 135.5±0.5 MHz), which disagrees with a simple SE model. A wider linewidth points to the presence of a cross-relaxation between ^{1}H and ^{19}F, such that a ^{19}F-DNP spectrum would have an additional contribution due to ^{1}H SE-DNP. Fitting the spectra with two Gaussians, however, produced very large variance in the fitted parameters, and therefore is not shown.

Discussion

Heteronuclear-DNP

In this work we observed the hn-DNP effect arising in the system containing ^{1}H and ^{19}F as polarizable nuclei and BDPA as a polarizing agent. The key observation supporting our assignment is a characteristic DNP spectrum where ^{1}H and ^{19}F have enhancements of opposite signs. Simulations based on a quantum mechanical model of heteronuclear thermal mixing provide a very good qualitative agreement with the experimental spectra. The enhancements of opposite sign around $\omega_e \pm (\omega_H - \omega_F)$ can also in principle arise from a double-SE, however, this has been ruled out based on the following observations:

- The double-SE DNP spectrum is expected to have additional lines at $\omega_e \pm (\omega_H + \omega_F)$, however, corresponding peaks are absent in our DNP spectra.
- Power dependence shows a linear increase of SE with power, while a different behaviour for hn-DNP was observed.

- The shape of the hn-DNP spectrum and its maximum enhancements and build-up times depend strongly on the concentration of electrons, pointing to the importance of electron dipolar couplings in the hn-DNP mechanism, which should not be in the case of double-SE.

We assign the observed hn-DNP as hn-TM based on the following evidence:

- Estimates of the electron T_{1e} combined with the extent of inhomogeneous broadening suggest that MW irradiation is most likely to saturate the entire ESR line, i.e. no significant hole-burning required for hn-CE can be produced in such a system.
- The measured shape of the ^{19}F-DNP spectra of the hn-DNP has a noticeable dependence on the concentration of BDPA and MW power. The simulations based on the hn-TM model provide good qualitative agreement with the experimental data in both cases, compared to less good agreement for hn-CE mechanism.

The hn-CE proposed earlier[19] and hn-TM explained in the "Theoretical Background" section are related to one another as regular CE and TM. The transfer of energy between the electron and nuclear spins in both hn-CE and hn-TM is based on the four-spin mechanism described previously[19], however the polarization gradient or the difference of polarization between the neighbouring electrons is created in a different manner. In CE, the polarization gradient is produced by irradiating individual electron spin in a pair, whereas in TM it is produced by the microwave irradiation of a system of many coupled electron spins.

At the same time, it is also important to point out, that while the existence of electron dipolar energy temperature needed for the thermal mixing has been confirmed experimentally by measuring saturated ESR lineshapes in systems such as paramagnetic impurities in single crystals as reviewed in ref. [38], to the best of our knowledge, for stable organic radicals used in modern DNP applications it was done only indirectly by comparing the spin temperatures of

polarizable nuclei in the system[12,13,15,39]. ELDOR measurements, probing the shape of the ESR line after the saturation would help to provide a more quantitative view of the observed hn-DNP effect[40], however that is beyond the scope of this work.

^{1}H-^{19}F cross-relaxation.

The mixing of electron and nuclear states in a four-spin model required for both hn-CE and hn-TM predicts the presence of a cross-relaxation between nuclei of different types in the absence of MW irradiation. Such cross-relaxation was observed via a recovery of saturated ^{19}F signals under the saturation of ^{1}H nuclei. The presence of nuclear cross-relaxation was further supported by the magnetization recovery experiment and ^{19}F-DNP spectra.

It is important however, to rule out three other cross-relaxation mechanisms produced by the presence of electrons:

1. The regular TM model predicts the indirect interaction between the nuclear Zeeman reservoirs of ^{1}H and ^{19}F via an electron dipolar energy reservoir. In our system such contact is rather unlikely, because the Larmor frequencies of ^{1}H and ^{19}F are much bigger compared to the ESR linewidth.
2. Rapidly relaxing paramagnetic species are known to induce nuclear relaxation[41] due to the electron spin flips caused by the interaction of electron spins with the lattice (T_{1e}-driven process) or by dipole-dipole interaction between electron spins (T_{2e}-driven process). The rate of induced nuclear relaxation affecting R_F depends on fluctuating $\hat{S}_z\hat{J}_{\pm}$ terms, making R_F proportional to the non-secular hyperfine $\sim\left|B^{(F)}\right|^2$ of the electron-nucleus system[41]. In a similar manner, the electron relaxation may also involve terms $\hat{S}_z\hat{J}_{\pm}\hat{I}_{\mp}$ leading to a flip-flop of two nuclei, one ^{1}H and one ^{19}F, which produce the cross-relaxation between ^{1}H and ^{19}F, and affect the rate σ. Since the probability of the "forbidden" transitions involving a flip of two nuclei depends on the hyperfine and

Larmor frequencies in the higher order of perturbation theory[19,30], such an effect is expected to be significantly weaker. In other words, the increase in R_F rate due to increase in BDPA concentration would be greater than the induced increase in σ. This in turn, disagrees with experimental data shown in Table 3 thus allowing to rule out this mechanism. Furthermore, the cross-relaxation rate σ in a sample containing 40 mM TEMPO is significantly faster compared to BDPA, while the R_F rates are almost the same in both samples, again pointing to the fact that R_F and σ cannot be induced by the same electron relaxation process.

3. Another type of cross-relaxation process may come from spin diffusion between ^{1}H and ^{19}F assisted by large hyperfine couplings, or in other words, when paramagnetically broadened NMR spectra of ^{1}H and ^{19}F overlap. Fluctuations of electron spin orientation due to a T_{1e} or T_{2e}-driven process may temporarily bring into resonance ^{1}H and ^{19}F nuclei producing effective spin-diffusion via a dipolar interaction between them[42]. However, since the nuclear Larmor frequencies at the magnetic field of 3.4 T are separated by 8.4 MHz, this process requires involvement of nuclei with rather large hyperfine couplings. Pulsed electron nuclear double resonance (ENDOR) measurements reveal the largest hyperfine coupling for ^{1}H as 7.7 MHz[29], whereas matrix ^{1}H nuclei have couplings smaller than 1 MHz. Since the Larmor frequencies of ^{19}F and ^{1}H are similar, the hyperfine couplings the matrix ^{19}F nuclei can also be estimated as 1 MHz. Such small matrix ^{19}F hyperfine couplings agree with a rather significant delocalization of unpaired electron spin density over the BDPA molecule[32]. Since the ENDOR frequencies $\omega_{1,2}$ for a spin ½ nucleus coupled via a hyperfine coupling A are $\omega_{1,2} = \omega_0 \pm A/2$, where ω_0 is the nuclear Larmor frequency, it is clear that ^{19}F and ^{1}H ENDOR spectra in BDPA should not overlap. Therefore, spin diffusion

between ^{1}H and ^{19}F assisted by the hyperfine couplings is unlikely at the magnetic field of 3.35 T used in our experiments.

The rate of cross-relaxation σ in TEMPO compared to BDPA is faster, which cannot be explained well at our current level of understanding. In a sample with a broad ESR line the probability of finding a "good" pair of electrons satisfying the matching condition $|\omega_{1e} - \omega_{2e}| \approx |\omega_F - \omega_H|$ should be smaller, yielding smaller observed cross-relaxation rate σ, in contrast with our observations. However, the rate of polarization transfer depends on the hyperfine couplings, due to the factor $\frac{DB_H B_F}{\omega_H \omega_F}$ shown in eqn (9). As pointed out earlier, the unpaired electron spin density in BDPA is delocalized over many atoms, leading to small hyperfine couplings with matrix ^{19}F and ^{1}H nuclei. In contrast, in the TEMPO radical, the spin density is partitioned almost equally between the nitrogen and oxygen atoms of the NO fragment, which may lead to bigger couplings with nearby nuclei[43]. Therefore, while the likelihood of finding a suitable pair of electrons is smaller for TEMPO, the polarization transfer rates in TEMPO could be greater due to larger hyperfine couplings and may lead to a larger observed nuclear cross-relaxation rate.

Interestingly, a rather noticeable cross-relaxation is present even in the degassed sample without any polarizing agent. Two possible explanations for this can be offered. First, previous experiments in LiF crystals have revealed that energy reservoirs formed by the dipolar couplings of Li and F nuclei acquire the same temperature[44], and therefore saturation of one type of nuclei can be transferred to the other. Alternatively, the crosstalk may be caused by some other non-coherent cross-relaxation process and may be specific to the molecular structure of the matrix molecules. Recently it was found that a nuclear Overhauser effect-like cross-relaxation between ^{1}H and ^{13}C exists under conditions of solid state magic angle spinning DNP (magnetic field ~9.4T , temperature ~100 K)[45,46]. Such a mechanism requires a difference

in the rates, and effectively spectral densities, associated with double-quantum and zero-quantum relaxation. One potential process that might cause this at the temperature of 1.4 K could be the tunnelling of hindered methyl groups in toluene molecules [47]. However, a detailed investigation and thereby distinguishing between the two potential mechanisms goes beyond the scope of this work.

Conclusions.

This work provides the evidence of hn-DNP effects in a system with polarizable ^{19}F and ^{1}H nuclei. The observed characteristic ^{1}H and ^{19}F-DNP spectra arising due to hn-DNP were explained using a hn-TM mechanism, which is based on the presence of electron and nuclear states mixing in a four-spin system. The same state mixing is responsible for the cross-relaxation between ^{1}H and ^{19}F which occurs even without application of MW irradiation. The characteristic DNP spectrum arising due to hn-DNP involving ^{19}F and ^{1}H becomes distinguishable from the DNP spectra due to other mechanisms, because of a small difference of nuclear Larmor frequencies, a rather narrow linewidth of BDPA and a small contribution of a regular thermal mixing of ^{1}H and ^{19}F to the DNP spectrum. While in our system the polarization gradient across the ESR line was caused by a thermal mixing mechanism, in principle, similar effects may be expected under conditions when hn-CE becomes dominant[20]. Understanding such heteronuclear phenomenona may be useful for determining the optimal conditions for DNP in other ^{19}F-containing samples, both under conditions of dissolution DNP[48] and solid state magic angle spinning NMR DNP[49]. Furthermore, hn-TM and the associated cross-relaxation phenomena might potentially be found in other heteronuclear systems under DNP conditions.

Acknowledgements

We would like to thank Nathan Woodhouse and Caitlin Hardie for their help in constructing the double-tuned circuit of the NMR probe. This project was funded by the EU Horizon 2020 programme under the Marie Sklodovska-Curie grant No 642773 (EUROPOL ITN) and EPSRC grant EP/N03404X/1 to WK.

References.

1 A. S. L. Thankamony, J. J. Wittmann, M. Kaushik and B. Corzilius, *Prog. Nucl. Magn. Reson. Spectrosc.*, 2017, **102**–**103**, 120–195.

2 G. Zhang and C. Hilty, *Magn. Reson. Chem.*, 2018, **56**, 566–582.

3 K. M. Brindle, S. E. Bohndiek, F. A. Gallagher and M. I. Kettunen, *Magn. Reson. Med.*, 2011, **66**, 505–519.

4 A. Abragam and M. Goldman, *Reports Prog. Phys.*, 1978, **41**, 395–467.

5 V. A. Atsarkin, *Sov. Phys. Uspekhi*, 1978, **21**, 725–745.

6 Y. Hovav, A. Feintuch and S. Vega, *J. Magn. Reson.*, 2010, **207**, 176–189.

7 C. D. Jeffries, *Phys. Rev.*, 1957, **106**, 164–165.

8 Y. Hovav, A. Feintuch and S. Vega, *J. Magn. Reson.*, 2012, **214**, 29–41.

9 W. de Boer, *J. Low Temp. Phys.*, 1976, **22**, 185–212.

10 V. A. Atsarkin and A. V. Kessenikh, *Appl. Magn. Reson.*, 2012, **43**, 7–19.

11 S. F. J. Cox, V. Bouffard and M. Goldman, *J. Phys. C Solid State Phys.*, 1973, **6**, L100–L103.

12 M. Borghini and K. Scheffler, *Phys. Rev. Lett.*, 1971, **26**, 1362–1365.

13 M. Borghini, *Phys. Rev. Lett.*, 1968, **20**, 419–421.

14 L. Lumata, A. K. Jindal, M. E. Merritt, C. R. Malloy, A. D. Sherry and Z. Kovacs, *J. Am. Chem. Soc.*,

2011, **133**, 8673–8680.

15 L. Lumata, M. Merritt, C. Malloy, A. D. Sherry and Z. Kovacs, *Appl. Magn. Reson.*, 2012, **43**, 69–79.

16 W. de Boer, M. Borghini, K. Morimoto, T. O. Niinikoski and F. Udo, *J. Low Temp. Phys.*, 1974, **15**, 249–267.

17 Y. Hovav, A. Feintuch and S. Vega, *Phys. Chem. Chem. Phys.*, 2013, **15**, 188–203.

18 A. Karabanov, G. Kwiatkowski, C. U. Perotto, D. Wiśniewski, J. McMaster, I. Lesanovsky and W. Köckenberger, *Phys. Chem. Chem. Phys.*, 2016, **18**, 30093–30104.

19 D. Shimon, Y. Hovav, I. Kaminker, A. Feintuch, D. Goldfarb and S. Vega, *Phys. Chem. Chem. Phys.*, 2015, **17**, 11868–11883.

20 I. Kaminker, D. Shimon, Y. Hovav, A. Feintuch and S. Vega, *Phys. Chem. Chem. Phys.*, 2016, **18**, 11017–11041.

21 D. Shimon, Y. Hovav, A. Feintuch, D. Goldfarb and S. Vega, *Phys. Chem. Chem. Phys.*, 2012, **14**, 5729–5743.

22 D. Guarin, S. Marhabaie, A. Rosso, D. Abergel, G. Bodenhausen, K. L. Ivanov and D. Kurzbach, *J. Phys. Chem. Lett.*, 2017, **8**, 5531–5536.

23 J. Granwehr, J. Leggett and W. Köckenberger, *J. Magn. Reson.*, 2007, **187**, 266–276.

24 J. Ekin, *Experimental Techniques for Low-Temperature Measurements : Cryostat Design, Material Properties and Superconductor Critical-Current Testing*, Oxford University Press, Oxford, 2006.

25 A. V. Smorodin, A. S. Rybalko and D. Konstantinov, *J. Low Temp. Phys.*, 2017, **187**, 361–368.

26 J. Mispelter, M. Lupu and A. Briguet, *NMR probeheads for biophysical and biomedical experiments : theoretical principles and practical guidelines*, Imperial College Press, London, 2015.

27 M. D. Schnall, V. Harihara Subramanian and J. S. Leigh, *J. Magn. Reson.*, 1986, **67**, 129–134.

28 J. Granwehr and W. Köckenberger, *Appl. Magn. Reson.*, 2008, **34**, 355–378.

29 M. Bennati, C. T. Farrar, J. A. Bryant, S. J. Inati, V. Weis, G. J. Gerfen, P. Riggs-Gelasco, J. Stubbe and R. G. Griffin, *J. Magn. Reson.*, 1999, **138**, 232–243.

30 Y. Hovav, A. Feintuch and S. Vega, *J. Chem. Phys.*, 2011, **134**, 074509.

31 V. Weis and R. G. Griffin, *Solid State Nucl. Magn. Reson.*, 2006, **29**, 66–78.

32 N. S. Dalal, D. E. Kennedy and C. A. McDowell, *J. Chem. Phys.*, 1974, **61**, 1689–1697.

33 L. Lumata, Z. Kovacs, A. D. Sherry, C. Malloy, S. Hill, J. Van Tol, L. Yu, L. Song and M. E. Merritt, *Phys. Chem. Chem. Phys.*, 2013, **15**, 9800–9807.

34 A. Leavesley, D. Shimon, T. A. Siaw, A. Feintuch, D. Goldfarb, S. Vega, I. Kaminker and S. Han, *Phys. Chem. Chem. Phys.*, 2017, **19**, 3596–3605.

35 C. T. Farrar, D. A. Hall, G. J. Gerfen, S. J. Inati and R. G. Griffin, *J. Chem. Phys.*, 2001, **114**, 4922–4933.

36 S. Jannin, A. Comment and J. J. van der Klink, *Appl. Magn. Reson.*, 2012, **43**, 59–68.

37 I. Solomon, *Phys. Rev.*, 1955, **99**, 559–565.

38 V. A. Atsarkin and M. I. Rodak, *Sov. Phys. Uspekhi*, 1972, **15**, 251–265.

39 F. Kurdzesau, B. van den Brandt, A. Comment, P. Hautle, S. Jannin, J. J. van der Klink and J. A. Konter, *J. Phys. D. Appl. Phys.*, 2008, **41**, 155506.

40 Y. Hovav, D. Shimon, I. Kaminker, A. Feintuch, D. Goldfarb and S. Vega, *Phys. Chem. Chem. Phys.*, 2015, **17**, 6053–6065.

41 A. Abragam, *The principles of nuclear magnetism*, Oxford University Press, Oxford, 1961.

42 R. Tycko and G. Dabbagh, *Isr. J. Chem.*, 1992, **32**, 179–184.

43 P. J. Brown, A. Capiomont, B. Gillon and J. Schweizer, *Mol. Phys.*, 1983, **48**, 753–761.

44 M. E. Zhabotinskii, A. E. Mefed and M. I. Rodak, *JETP Lett.*, 1970, **11**, 328.

45 D. Daube, V. Aladin, J. Heiliger, J. J. Wittmann, D. Barthelmes, C. Bengs, H. Schwalbe and B. Corzilius, *J. Am. Chem. Soc.*, 2016, **138**, 16572–16575.

46 M. M. Hoffmann, S. Bothe, T. Gutmann, F. F. Hartmann, M. Reggelin and G. Buntkowsky, *J. Phys. Chem. C*, 2017, **121**, 2418–2427.

47 A. J. Horsewill, *Prog. Nucl. Magn. Reson. Spectrosc.*, 1999, **35**, 359–389.

48 Y. Kim and C. Hilty, *Angew. Chemie - Int. Ed.*, 2015, **54**, 4941–4944.

49 M. Lu, M. Wang, I. V. Sergeyev, C. M. Quinn, J. Struppe, M. Rosay, W. Maas, A. M. Gronenborn and T. Polenova, *J. Am. Chem. Soc.*, 2019, **141**, 5681–5691.

Figure Legend

Fig. 1 (A) Level diagram of the four-spin system consisting of a pair of electron spins and ^{1}H and ^{19}F nuclear spins. Dashed boxes enclose manifolds of electronic states $|\boldsymbol{\alpha_{1e}\alpha_{2e}}\rangle$,$|\boldsymbol{\beta_{1e}\beta_{2e}}\rangle$ and $|\boldsymbol{\alpha_{1e}\beta_{2e}}\rangle$ with $|\boldsymbol{\beta_{1e}\alpha_{2e}}\rangle$, which are separated from one another by electron Zeeman frequencies $\sim\boldsymbol{\omega_{1e}, \omega_{2e}}$. The energy levels within the manifolds are split by the combinations of ^{1}H and ^{19}F nuclear Zeeman frequencies $\boldsymbol{\omega_H}$ and $\boldsymbol{\omega_F}$ respectively. (B) The manifold of $|\boldsymbol{\alpha_{1e}\beta_{2e}}\rangle$ and $|\boldsymbol{\beta_{1e}\alpha_{2e}}\rangle$ levels at a higher resolution. The $|\boldsymbol{\alpha_{1e}\beta_{2e}\alpha_H\beta_F}\rangle$ and $|\boldsymbol{\beta_{1e}\alpha_{2e}\beta_H\alpha_F}\rangle$ states have very similar energies, when $|\boldsymbol{\omega_{1e} - \omega_{2e}}| \approx \boldsymbol{\omega_H - \omega_F}$. The degeneracy of these levels leads to a strong mixing between the corresponding states. (C) Level diagram for a pair of ^{1}H and ^{19}F nuclei interacting with a system of many dipolar coupled electrons. Dashed boxes enclose manifolds of levels with the same projection of the total electron spin angular momentum $\boldsymbol{M_S}$. The manifolds are separated by an electron Larmor frequency $\boldsymbol{\omega_e}$, and each manifold consists of four bands with a characteristic width $\boldsymbol{\Delta_{band}}$ corresponding to nuclear states $|\boldsymbol{\alpha_H\beta_F}\rangle$, $|\boldsymbol{\beta_H\alpha_F}\rangle$, $|\boldsymbol{\alpha_H\alpha_F}\rangle$, $|\boldsymbol{\beta_H\beta_F}\rangle$. (BLUE) and (GREEN) in all panels show the groups of levels corresponding to $|\boldsymbol{\alpha_H\beta_F}\rangle$ and $|\boldsymbol{\beta_H\alpha_F}\rangle$ respectively, (BLACK) shows groups of $|\boldsymbol{\alpha_H\alpha_F}\rangle$, $|\boldsymbol{\beta_H\beta_F}\rangle$.

Fig. 2 Experimental and simulated ^{1}H and ^{19}F-DNP spectra in a sample of 25/75 (% v/v) fluorobenzene/toluene containing [BDPA]=40 mM. (A) Experimental NMR signal intensity of ^{1}H- (RED) and ^{19}F-nuclei (BLACK) as a function of MW irradiation frequency offset $(\boldsymbol{\omega_{MW} - \omega_0})/\boldsymbol{2\pi}$. Signal is recorded after $\boldsymbol{t_{bu}}$ =30 s of build-up following a train of saturating RF pulses, used for destroying magnetization before each measurement. The signal intensity is normalized to its maximum value, the horizontal axis is offset by $\boldsymbol{\omega_0/2\pi}$=93.93 GHz. (B) Simulations of ^{1}H-(RED) and ^{19}F-DNP (BLACK) spectra under conditions shown in (A). (B, TOP LEFT) enhancements after $\boldsymbol{t_{bu}}$ =30 s, (B, TOP RIGHT) enhancements after $\boldsymbol{t_{bu}}$ =3000

s, (B, BOTTOM LEFT) normalized signals after $\boldsymbol{t_{bu}} = 30$ s, (B, BOTTOM RIGHT) normalized signals after $\boldsymbol{t_{bu}}$ =3000 s.

Fig. 3 Experimental and simulated ^{19}F-DNP spectra for various concentrations of BDPA in 25/75 (% v/v) fluorobenzene/toluene.(A) The NMR signal of ^{19}F-nuclei as a function of microwave frequency offset $(\boldsymbol{\omega_{MW} - \omega_0})/\boldsymbol{2\pi}$. The signal is recorded after $\boldsymbol{t_{bu}}$ =30 s of build-up following a train of saturating RF pulses, used for destroying magnetization before each measurement. The NMR signal strength is normalized to its maximum value, and the horizontal axis is offset by $\boldsymbol{\omega_0/2\pi}$=93.93 GHz. Only the region of $(\boldsymbol{\omega_{MW} - \omega_0})/\boldsymbol{2\pi}$ =-180…0 MHz was recorded for reducing the total experimental time. (BLACK) [BDPA]=40 mM, (RED) [BDPA]=30 mM, (GREEN) [BDPA]=20 mM. (B) Simulations of normalized ^{19}F-DNP spectra under conditions shown in (A) using hn-TM and SE models. (B, TOP) after a build-up t_{bu} =30 s, (B, BOTTOM) after a build-up t_{bu} =3000s. Color legend is the same as (A). (C) Simulations of normalized ^{19}F-DNP spectra as a function of [BDPA] using hn-CE model. (BLACK) [BDPA] = 40 mM, (RED) [BDPA] =30 mM, (GREEN) [BDPA]=20 mM, (DOTTED BLACK) [BDPA] = 8 mM, (DOTTED RED) [BDPA] = 4 mM.

Fig. 4 Experimental and simulated ^{19}F DNP spectra at various levels of MW power in a sample of 25/75 (% v/v) fluorobenzene/toluene containing [BDPA]=40 mM. (A) The signal of ^{19}F-nuclei as a function of MW irradiation frequency offset $(\omega_{MW} - \omega_0)/2\pi$. The signal is recorded after t_{bu} =100 s of build-up following a train of saturating RF pulses, used for destroying magnetization before each measurement. Signal intensity is normalized to its maximum value at 400 mW, the horizontal axis is offset by $\omega_0/2\pi$ =93.93 GHz. (B) Simulations of ^{19}F-signal enhancements at various MW power levels using heteronuclear thermal mixing model. (C) Simulations of ^{19}F-signal intensity at various MW power levels using heteronuclear cross-effect model. Legend is the same as in panel (B).

Fig. 5 (A) Saturation-recovery experiment with RF pulse saturation at a frequency ω_{sat}, the time interval between the saturation of ^{19}F nuclei and the read-out pulse is incremented by increasing the number N of 250 ms blocks, consisting of one $\pi/2$ pulse at ω_{sat}. (B) Saturation-recovery build-up curves for ^{19}F-nuclei in a sample of degassed 25/75 (% v/v) fluorobenzene/toluene without paramagnetic dopant. FILLED symbols mark build-up curves recorded in an interleaved experiment with (FILLED BLACK) and without saturation (FILLED RED) on the ^{1}H Larmor frequency of $\omega_{sat}/2\pi$ =142.7 MHz. EMPTY symbols mark build-up curves recorded in an interleaved experiment with (EMPTY BLACK) and without (EMPTY RED) saturation at a frequency of $\omega_{sat}/2\pi$ =138 MHz.

Tables

Table 1 Common parameters used for simulations of DNP data

Parameter	Value
Temperature, T	1.5 K
Magnetic field, B_0	3.4 T
T_{1e}	0.5 s
T_{2e}	10 us
$B^{(H)}$	7 MHz
$B^{(F)}$	2.5 MHz
D (for [BDPA]=40 mM)	0.3 MHz^3
ESR line FWHH (for [BDPA =40 mM]), A	27 MHz
dispersion parameter, d (for [BDPA]=40mM)	9 MHz

Table 2 Summary of enhancements and build-up times for solid effect and hn-DNP effects for various concentrations of BDPA. Unless mentioned otherwise, all measurements were carried out at full MW power of 400 mW.

BDPA concentration, mM	Nucleus	Solid Effect(SE) DNP		Heteronuclear DNP (hn-DNP)		Thermal signal
		enhancement	build-up time, s	enhancement	build-up time,s	build-up time,s
20	^{19}F	4.6±0.2	310±11	-1.3±0.1	447±41	259±7
	^{1}H	-	-	-	-	-
30	^{19}F	8.3±0.2	215±13	-3.0±0.2	244±8	260±8
	^{19}F (100 mW)	2.3±0.1	227±5	-2.2±0.1	203±3	260±8
	^{1}H	5.6±0.2	90±8	-	-	60±3
40	^{19}F	7.9±0.3	240±22	-3.4±0.2	162±10	232±6
	^{1}H	12.2±0.7	109±3	1.7±0.1	67±4	102±14

Table 3 Summary of ^{19}F relaxation rates $\boldsymbol{R_F}$, and cross-relaxation rates $\boldsymbol{\sigma}$ for various concentrations of paramagnetic species.

Sample	$1/R_F$, s^{-1}	$1/\sigma$, s^{-1}
40 mM BDPA	540±21	370±20
30 mM BDPA	397±9	447±14
20 mM BDPA	560±18	505±21
40 mM TEMPO	448±21	147±10
0 mM BDPA	636±10	892±20
0 mM BDPA degassed	1029±41	1044±56

Figure 1.

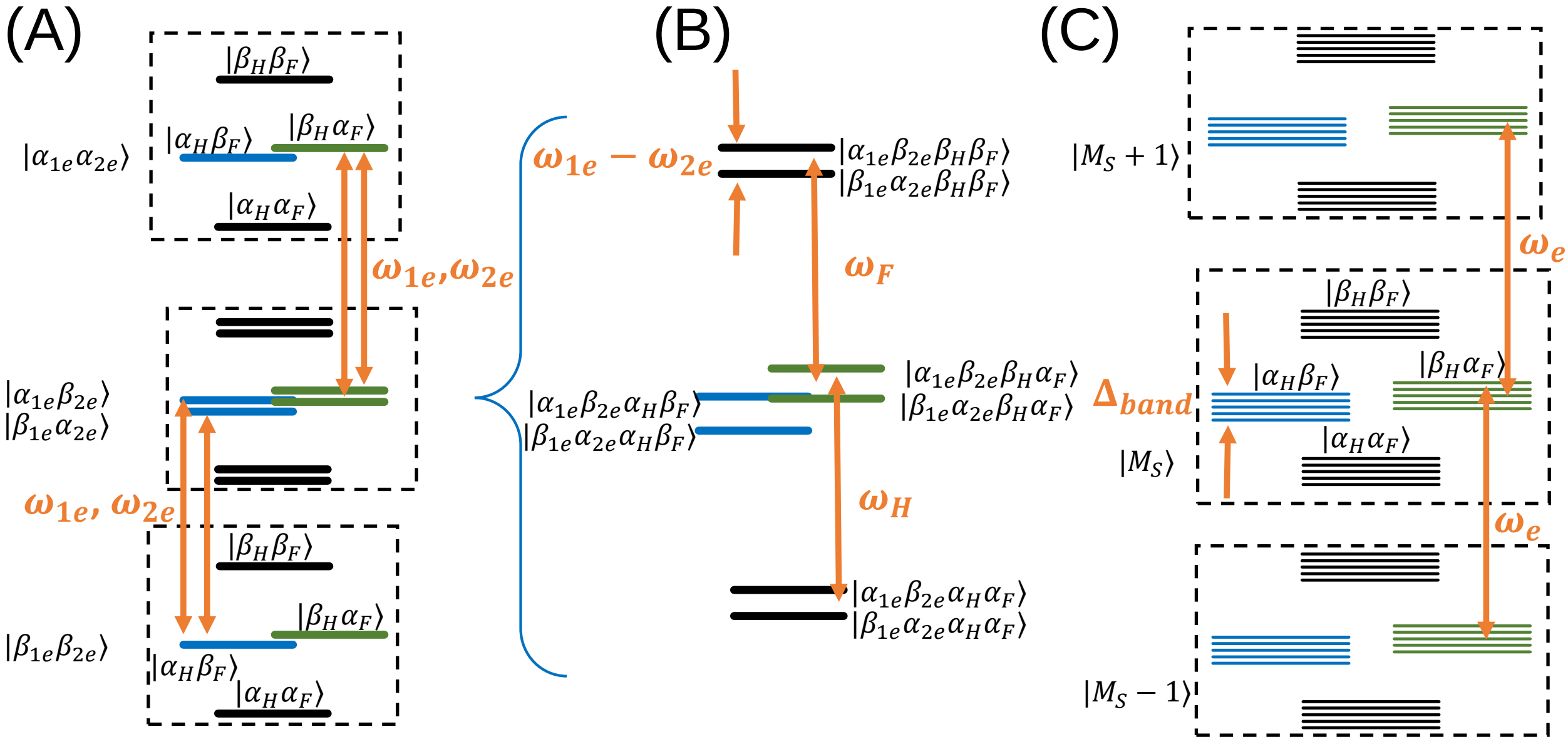
(A)
$|\beta_H\beta_F\rangle$
$|\alpha_H\beta_F\rangle$
$|\beta_H\alpha_F\rangle$
$|\alpha_H\alpha_F\rangle$
$|\alpha_{1e}\alpha_{2e}\rangle$
ω_{1e},ω_{2e}
$|\alpha_{1e}\beta_{2e}\rangle$
$|\beta_{1e}\alpha_{2e}\rangle$
ω_{1e}, ω_{2e}
$|\beta_H\beta_F\rangle$
$|\beta_H\alpha_F\rangle$
$|\beta_{1e}\beta_{2e}\rangle$
$|\alpha_H\beta_F\rangle$
$|\alpha_H\alpha_F\rangle$
(B)
$\omega_{1e} - \omega_{2e}$
$|\alpha_{1e}\beta_{2e}\beta_H\beta_F\rangle$
$|\beta_{1e}\alpha_{2e}\beta_H\beta_F\rangle$
ω_F
$|\alpha_{1e}\beta_{2e}\beta_H\alpha_F\rangle$
$|\alpha_{1e}\beta_{2e}\alpha_H\beta_F\rangle$
$|\beta_{1e}\alpha_{2e}\beta_H\alpha_F\rangle$
$|\beta_{1e}\alpha_{2e}\alpha_H\beta_F\rangle$
ω_H
$|\alpha_{1e}\beta_{2e}\alpha_H\alpha_F\rangle$
$|\beta_{1e}\alpha_{2e}\alpha_H\alpha_F\rangle$
(C)
$|M_S + 1\rangle$
ω_e
$|\beta_H\beta_F\rangle$
$|\alpha_H\beta_F\rangle$
$|\beta_H\alpha_F\rangle$
Δ_{band}
$|M_S\rangle$
$|\alpha_H\alpha_F\rangle$
ω_e
$|M_S - 1\rangle$

Figure 2.

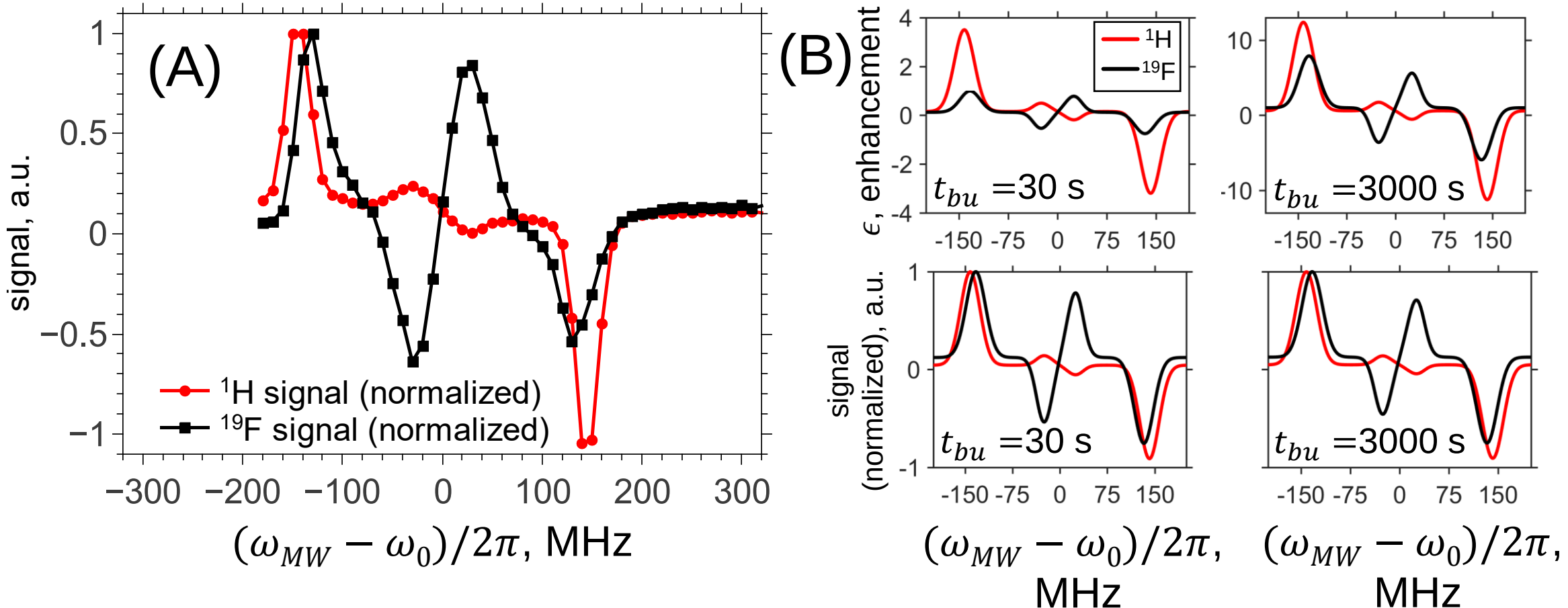
(A)
signal, a.u.
1
0.5
0
−0.5
−1
−300 −200 −100 0 100 200 300
$(\omega_{MW} - \omega_0)/2\pi$, MHz
^{1}H signal (normalized)
^{19}F signal (normalized)
(B)
ϵ, enhancement
4
2
0
-2
-4
^{1}H
^{19}F
t_{bu} =30 s
t_{bu} =3000 s
10
0
-10
-150 -75 0 75 150
signal (normalized), a.u.
1
0
-1
$(\omega_{MW} - \omega_0)/2\pi$, MHz
$(\omega_{MW} - \omega_0)/2\pi$, MHz

Figure 3.

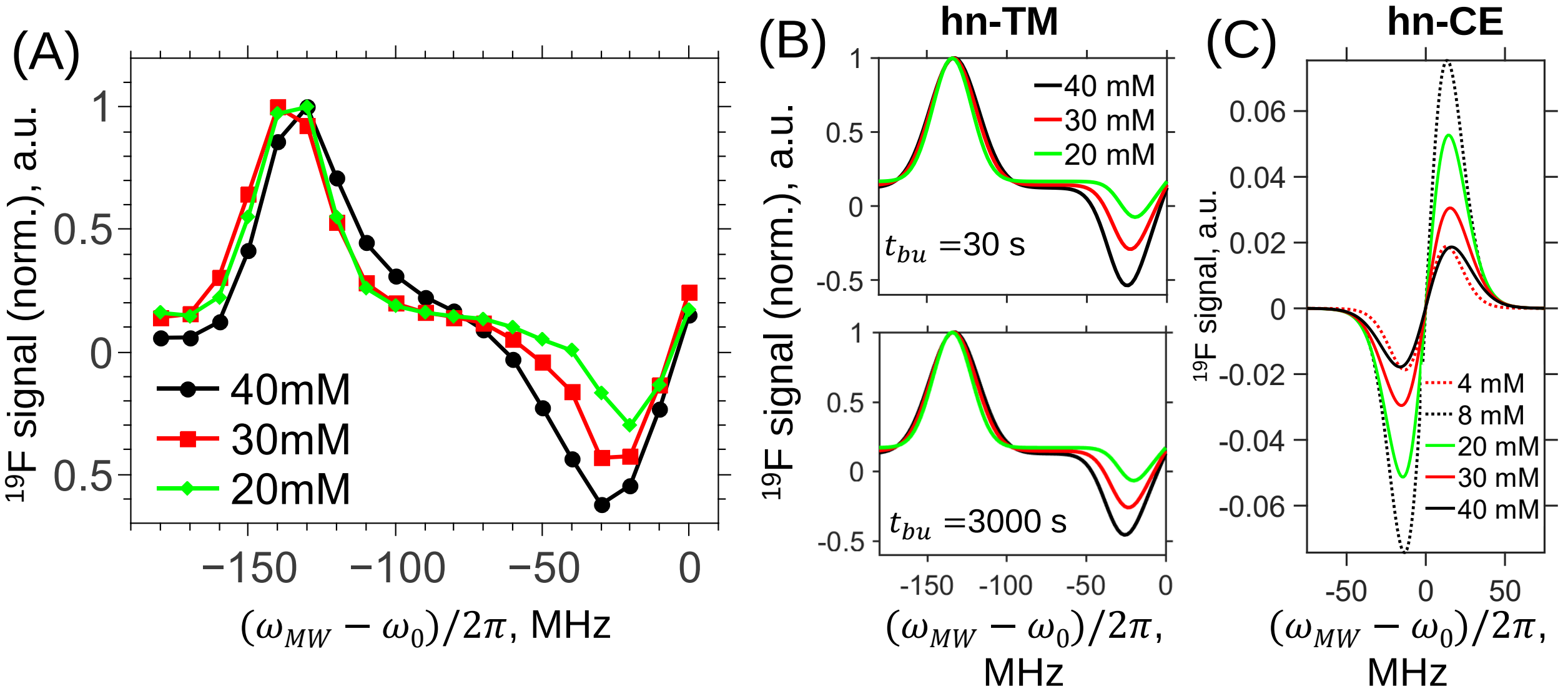
(A)
^{19}F signal (norm.), a.u.
1
0.5
0
0.5
40mM
30mM
20mM
−150
−100
−50
0
$(\omega_{MW} - \omega_0)/2\pi$, MHz
(B)
hn-TM
^{19}F signal (norm.), a.u.
1
0.5
0
-0.5
40 mM
30 mM
20 mM
t_{bu} =30 s
t_{bu} =3000 s
-150
-100
-50
0
$(\omega_{MW} - \omega_0)/2\pi$, MHz
(C)
hn-CE
^{19}F signal, a.u.
0.06
0.04
0.02
0
-0.02
-0.04
-0.06
4 mM
8 mM
20 mM
30 mM
40 mM
-50
0
50
$(\omega_{MW} - \omega_0)/2\pi$, MHz

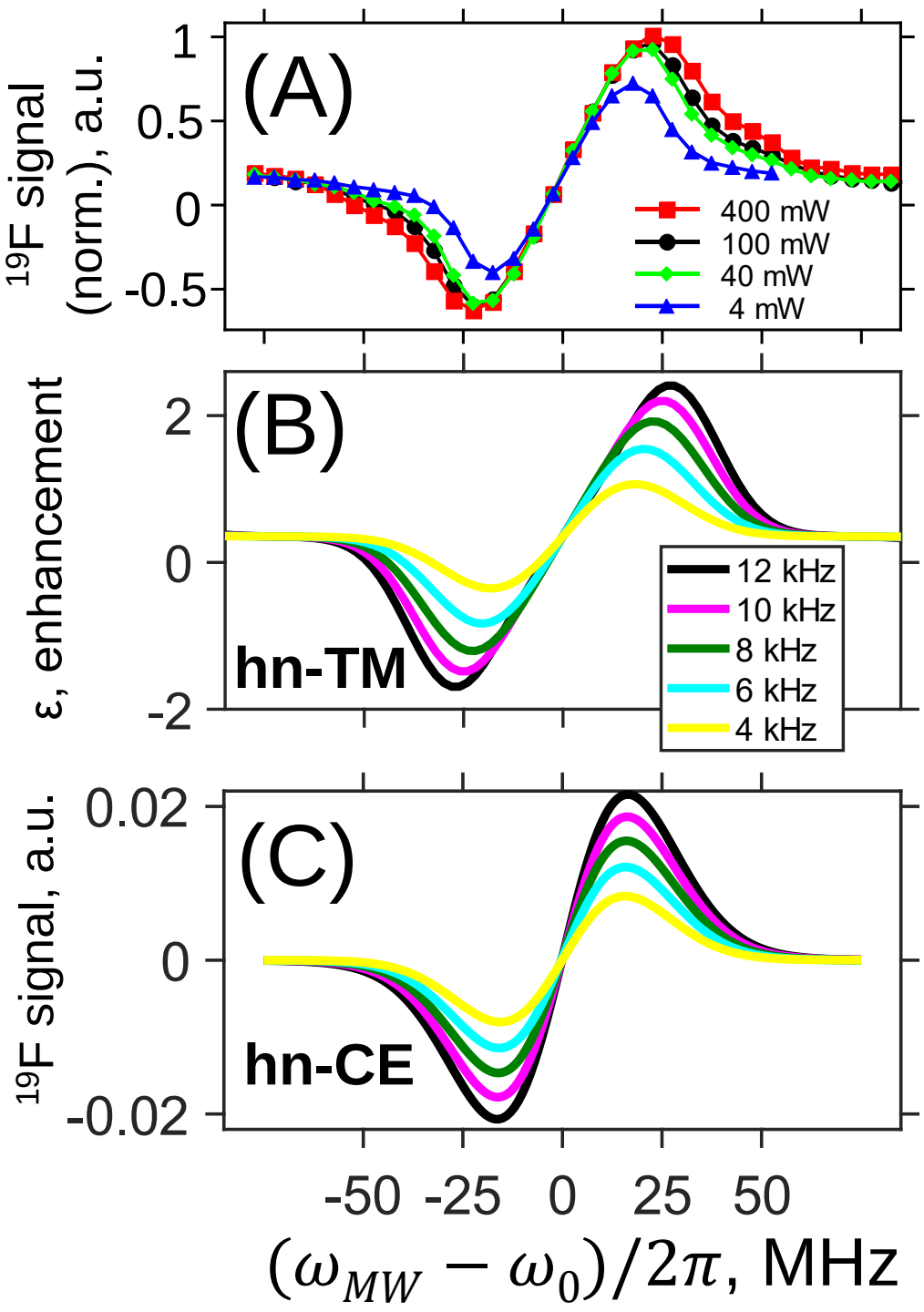
(A)
^{19}F signal (norm.), a.u.
1
0.5
0
-0.5
400 mW
100 mW
40 mW
4 mW
(B)
ε, enhancement
2
0
-2
hn-TM
12 kHz
10 kHz
8 kHz
6 kHz
4 kHz
(C)
^{19}F signal, a.u.
0.02
0
-0.02
hn-CE
-50
-25
0
25
50
$(\omega_{MW} - \omega_0)/2\pi$, MHz

Figure 4.

Figure 5.

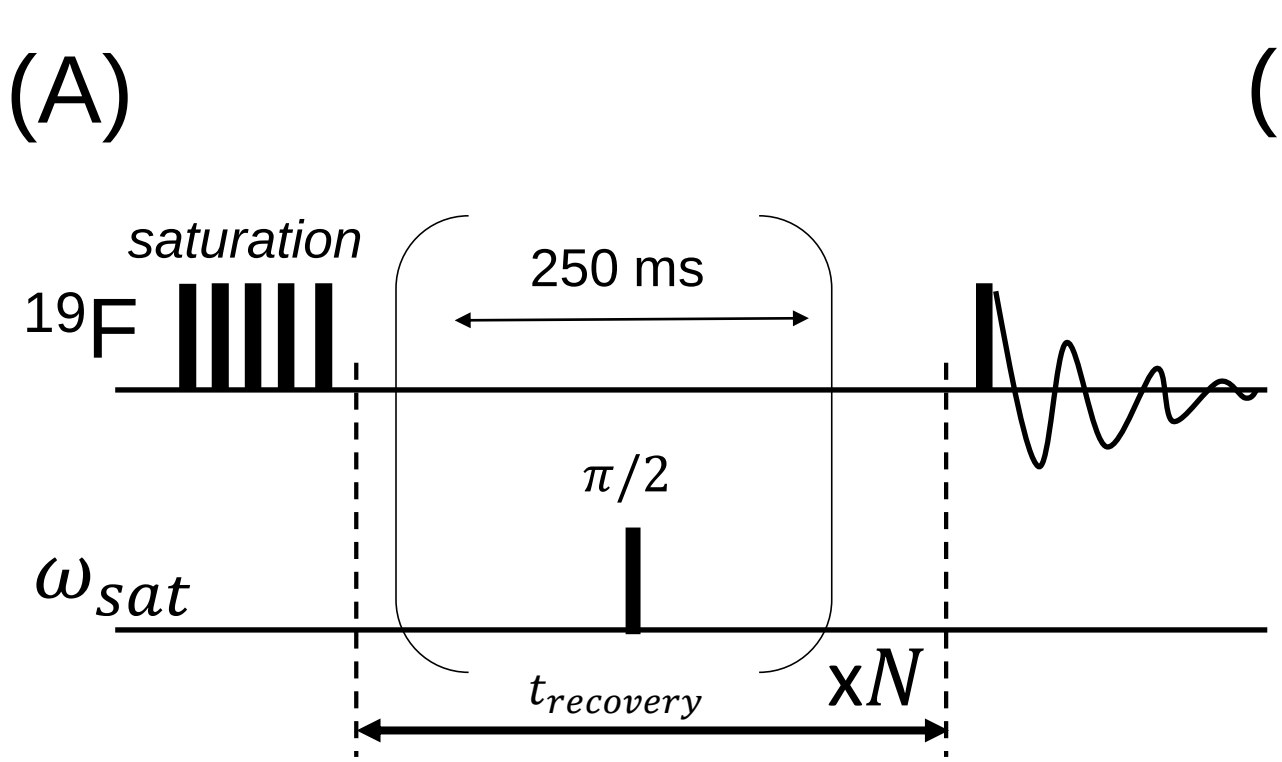
(A)
saturation
^{19}F
250 ms
$\pi/2$
ω_{sat}
$t_{recovery}$
xN

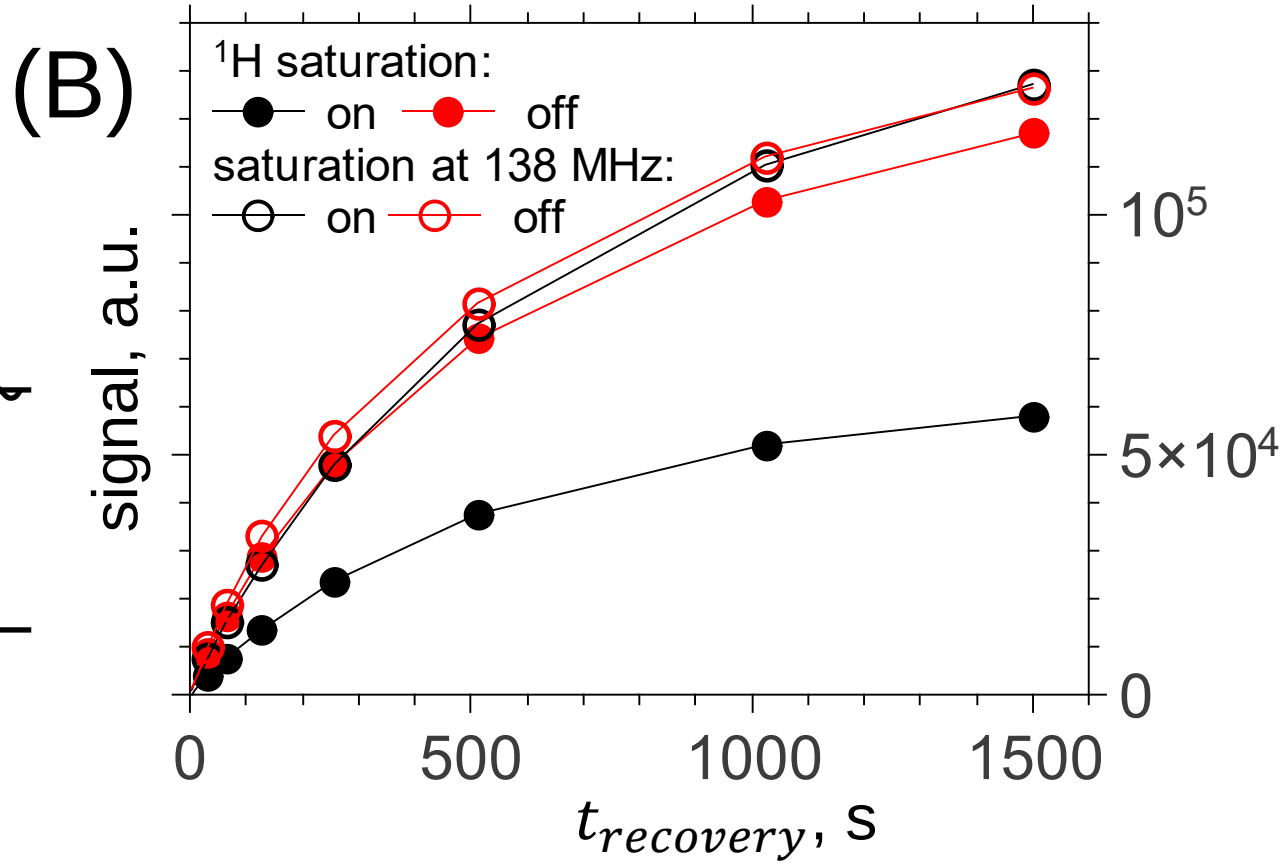
(B)
^{1}H saturation:
on
off
saturation at 138 MHz:
on
off
signal, a.u.
10^5
5×10^4
0
0
500
1000
1500
$t_{recovery}$, s